Design of a Compton transmission polarimeter

Fernandes Neres Benjamin
M1 Energy and nuclear engineering
Academic Year 2020/2021

VOUTIER Eric
Research Director
Laboratoire de Physique des 2 Infinis Irène Joliot-Curie
Université Paris Saclay, CNRS/IN2P3
15 Rue Georges Clémenceau, 91400 Orsay

Aknowledgement

I would like to thank **GRAMES Joe** and **SULEIMAN Riad** for our discussions about the polarimeter. Thank you for trying to organize a trip to the United States so I could discover the differents Hall of the Jefferson Lab.

I would also like to thank **HABET Sami** for his invaluable help.

Thanks to **HOBALLAH Mostafa** for his help and patience in answering my questions.

More generally, I would like to thank the entire **JLab/EIC** team for their welcome.

Finally, I would like to thank my internship supervisor **VOUTIER Eric** for having accepted my application, for all the interesting discussions we had, for his involvement during the internship and as well as the meticulous final proofreading of this report.

Abstract

Polarized lepton beams are essential tools for the study of the internal structure and dynamics of hadrons. In this quest, polarized positron beams are still very expensive to produce. In 2012, the PEPPo collaboration succeeded in demonstrating a novel and widely accessible technique allowing for the production of polarized positrons from polarized electrons of the order of a few MeV. During the experiment, the polarization of the electrons and positrons were measured with a Compton transmission polarimeter, which operation is based on the absorption of circularly polarized photons within a polarized target. This internship proposes the design of a new polarimeter to be used at Jefferson Lab for the measurement of the polarization of the electron beam at injector energies (5-10 MeV), as well as at the Brookhaven National Laboratory in the characterization of a new polarized electron source.

Laboratoire de Physique des 2 Infinis Irène Joliot-Curie

The Laboratoire de Physique des 2 Infinis Irène Joliot-Curie (IJCLab) is located on the campus of the Faculty of Science in Orsay.

The lab was created on January 2020 from the association of five former insitutes: the Centre for Nuclear and Material Sciences (CSNSM), the Laboratory for Neurobiology and Cancer Imaging and Modelling (IMNC), the Institut de Physique Nucléaire d'Orsay (IPNO), the Linear Accelerator Laboratory (LAL) and the Theoretical Physics Laboratory (LPT).

The laboratory focuses its research on the physics of the two infinites. It comprises 1 engineering pole and 7 research poles: Astroparticle - Astrophysics and Cosmology, Physics of Accelerators, High Energy Physics, Nuclear Physics, Theoretical Physics, Energy and environment, Health Physics.

The laboratory is a mixed entity of the Centre National de la la Recherche Scientifique, the University Paris-Saclay, and the University of Paris. A large part of its mission is also dedicated to teaching and training of future researchers.

This internship took place within the High Energy Physics pole, in the JLab/EIC team.

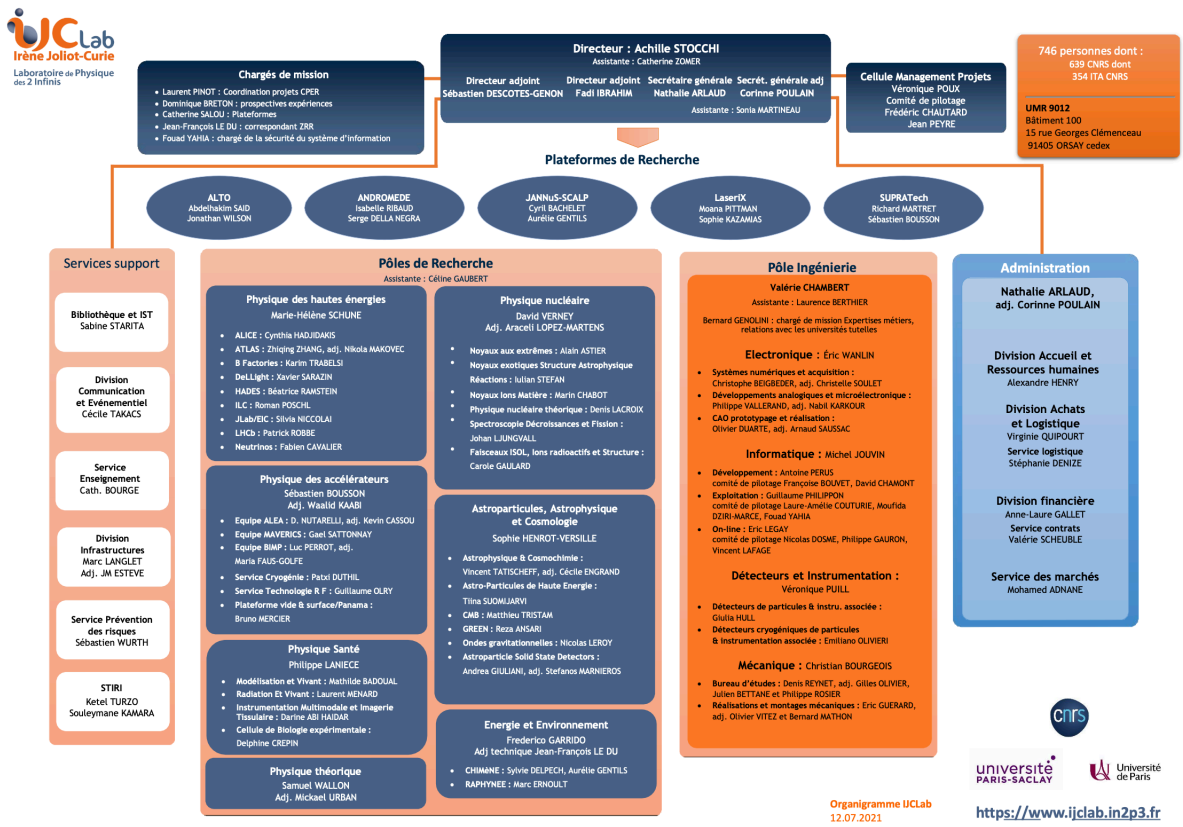

Figure 1: Organization of the laboratory.

Contents

List of Figures

List of Tables

1 Introduction

The study of the internal structure of hadrons allows a better understanding of the interactions between partons, that are the quarks and the gluons. Elastic electron scattering by the nucleon provides information on the spatial distribution of quarks while inelastic scattering provides information on the momentum distribution of partons. Generalized parton distributions (GPDs) are the elementary bricks of a recent theoretical framework which unifies these distributions within a unique parameterization deduced from the correlations of the parton position and momentum [1]. The current experimental program in this research field aims at the first results on the shape of these multi-dimensional distributions. The Deeply Virtual Compton Scattering (DVCS) is the simplest physics mechanism related to GPDs. It corresponds to the scattering of an electron off a nucleon through the exchange of a virtual photon with the re-emission of a real photon. Polarized beams of electrons and positrons are essential elements for accessing GPDs through DVCS and other related processes [2].

Many of the physics experiments require an accurate knowledge of the polarization of the incident beam. This is achieved with polarimeter devices such as a Mott polarimeter. For instance, Jefferson Lab (JLab) uses a Mott Polarimeter operating at the CEBAF (Continuous Electron Beam Accelerator Facility) injector at 5.5 MeV, and Compton polarimeters in the experimental halls operating at several GeV beam energies. There is a need to develop new methods to measure the polarization of particles for different energies using different physics processes in order to get redundant number of equipments for a more precise determination of the polarization of the beam. A Compton transmission polarimeter [3] was used in 2012 at JLab during the PEPPo experiment [4]. This polarimeter is based on the absorption of circularly polarized photons within a polarized target, and is composed of three main elements: a radiator, an analyzer, and a calorimeter.

This intership focuses on the design of a new Compton transmission polarimeter. The first part of this report is dedicated to the description of the physics processes and the mechanism of the polarization transfer. The second part concerns a rough theoretical modeling of the polarimeter while the third deals with the optimization of the calorimeter and of the analyzer. Another part concerns the experimental characterization of a BGO crystal, and the last part focuses on somes practical aspects of the operation of the Compton transmission polarimeter in the context of planned experiments.

2 Polarization phenomena in electromagnetic processes

The experimental signal of a Compton transmission polarimeter is the energy deposited in a detector by photons passing through an analyzer. These photons are initially generated in a radiator where incident electrons develop an electromagnetic shower which consists of photons, electrons, and positrons. Energetic electrons and positrons primarily emit photons according to the bremsstrahlung radiaton process. The emitted photons interact with matter primarily converting into an e^+e^--pair. These two processes continue till the pair-production threshold (1.022 MeV), leading to a cascade of particles. This paragraph focuses on electron- and photon-interactions with matter and the electron-to-photon transfer of polarization during the bremsstrahlung interaction.

2.1 Electromagnetic processes

2.1.1 Bremsstrahlung radiation

When electrons hit a target, they are deflected by the electric field of the target's nuclei. As a consequence, the fast moving electron is decelerated in the Coulomb field of the nucleus. The kinetic energy lost by the initial electron during the interaction is transformed into real photons. This phenomenon is referred in the literature as the bremsstrahlung radiation [5]. In the full screening approximation, valid for electrons with high total energy E and photon momenta $k \neq E$, the momentum differential cross section of this phenomenon can be expressed as [5]

$$\frac{d\sigma}{dk} = \frac{4\alpha r_0^2}{k}\left[\left(\frac{4}{3} - \frac{4y}{3} + y^{2)}\right)\left[Z^2(L_{rad} - f) + ZL'_{rad}\right] + \frac{1}{9}(1-y)\left(Z^2 + Z\right)\right] \tag{1}$$

where α is the fine structure constant, r_0 is the classical electron radius, and $y{=}k/E$. L_{rad}, L'_{rad} and f are Z-material dependent function defined as

$$L_{rad} \equiv L_{rad}(Z) = \ln(184.15\, Z^{-1/3}) \tag{2}$$

$$L'_{rad} \equiv L'_{rad}(Z) = \ln(1194\, Z^{-2/3}) \tag{3}$$

$$f \equiv f(Z) = 1.202\, Z - 1.0369\, Z^2 + \frac{1.008\, Z^3}{1+Z}\,. \tag{4}$$

L_{rad} and L'_{rad} are the radiation logarithms for Thomas-Fermi-Moliere atoms [5] and f is the Coulomb correction taking into account mechanisms beyond the one-photon exchange approximation. The bremsstrahlung photon spectra is a continuum in energy up to the kinetic energy of initial electrons. It is dominated by the emission of very low energy photons, as illustrated on Fig. 2 for 10 MeV electrons incident on copper.

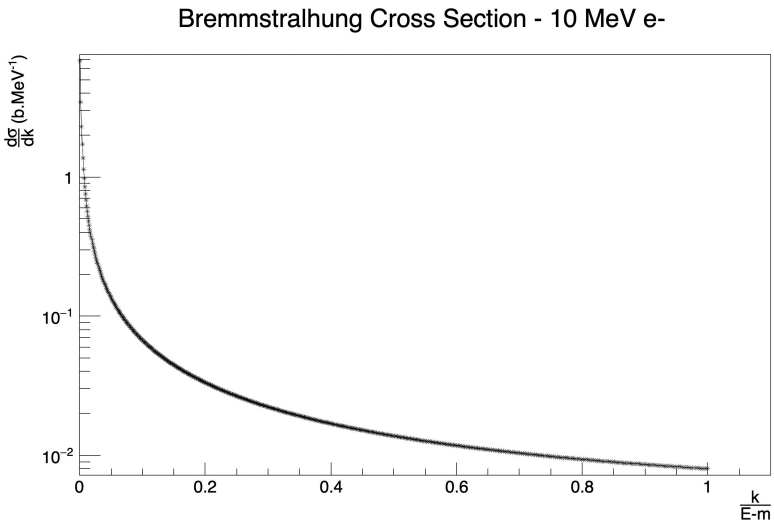

Figure 2: Bremsstrahlung differential cross section for a 10 MeV electron beam incident on a copper nucleus ($Z{=}29$); m denotes the electron mass.

2.1.2 Photo-electric effect

The photo-electric effect corresponds to the expulsion of atomic electrons by a photon interacting with an atom. Following the particle wave duality of the light, this phenomenon can be seen equivalently as a collision between a photon and a bound electron, or the resonant absorption of a wave by the atomic electron which is then emitted by the atom. The cross section for this process has been parameterized as [6]

$$\sigma_{\gamma e}(Z,k) = \frac{A_1(Z,k)}{k} + \frac{A_2(Z,k)}{k^2} + \frac{A_3(Z,k)}{k^3} + \frac{A_4(Z,k)}{k^4} \tag{5}$$

where the index denotes the first four electronic layers of the atom. The constant coefficients are material- and photon energy-dependent. This phenomenon discovered in 1887 by H. Hertz was ultimately explained in 1905 by A. Einstein who received in 1921 the Nobel Prize in Physics for this founding work of quantum physics.

2.1.3 Compton scattering

The Compton scattering corresponds to the collision of a photon with an electron: the photon bounces off the electron and loses energy. This reaction was discovered in 1922 by A. Compton who received in 1927 the Nobel Prize for this discovery.

Compton collisions can be considered as elastic collisions between photons and electrons. The photon is not absorbed in the process. The photon that emerges after interaction, so-called *scattered* photon, shares the initial energy with the moving electron. The scattered photon usually emerges in a different direction from the incident photon and can even go backwards, corresponding to the Compton back-scattering. The angular distribution of the scattered photons is described by the so-called Klein Nishina formula representing the doubly differential cross section

$$\frac{d^2\sigma_C^0}{d\theta d\phi} = \frac{1}{2}\left(r_0\frac{k}{k_0}\right)^2\left[\frac{k_0}{k}+\frac{k}{k_0}-\sin^2(\theta)\right]\sin(\theta)\,, \tag{6}$$

where (θ, ϕ) are the spherical diffusion angles of the photon, and $k_0(k)$ is the energy of the initial(scattered) photon expressed in units of the electron mass.

2.1.4 Pair Creation

The intense electric field surrounding the nucleus can transform an incident photon in an e^+e^--pair. The production of pairs in the $\gamma+A$ reaction can only take place if the photons have enough energy to produce at minima the pair at rest, that is larger than 1.022 MeV. This process is reciprocal to bremsstralhung and is described by similar equations. Its cross section can be parameterized as [6]

$$\sigma_{e^+e^-}(Z,k) = Z(Z+1)\left[F_1(X)+F_2(X)Z+\frac{F_3(X)}{Z}\right] \tag{7}$$

where

$$F_1(X) = a_0 + a_1X + a_2X^2 + a_3X^3 + a_4X^4 + a_5X^5 \tag{8}$$
$$F_2(X) = b_0 + b_1X + b_2X^2 + b_3X^3 + b_4X^4 + b_5X^5 \tag{9}$$
$$F_3(X) = c_0 + c_1X + c_2X^2 + c_3X^3 + c_4X^4 + c_5X^5\,, \tag{10}$$

with

$$X = \ln\left(\frac{k}{m}\right). \tag{11}$$

The (a_i, b_i, c_i) coefficients depend on the material where the conversion takes place.

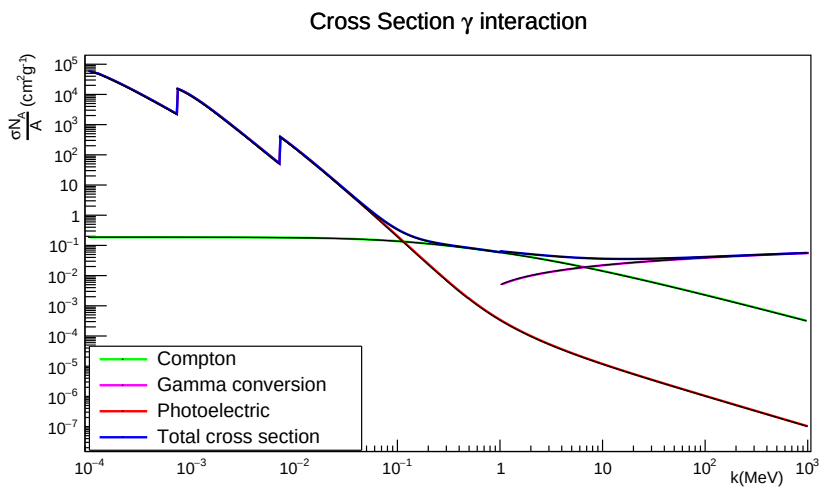

Figure 3: Interaction probability of photons with matter.

The probability of observing the photo-electric effect, the Compton scattering or the creation of an e^+e^--pair depends on the energy of the photon (Fig. 3). At low energy (a few keV), the most probable interaction is the photo-electric process. In the MeV range, the Compton interaction dominates the reaction mechanisms, while at higher energies the pair creation is essentially the only relevant interaction mechanism.

2.2 Electron-to-photon polarization transfer

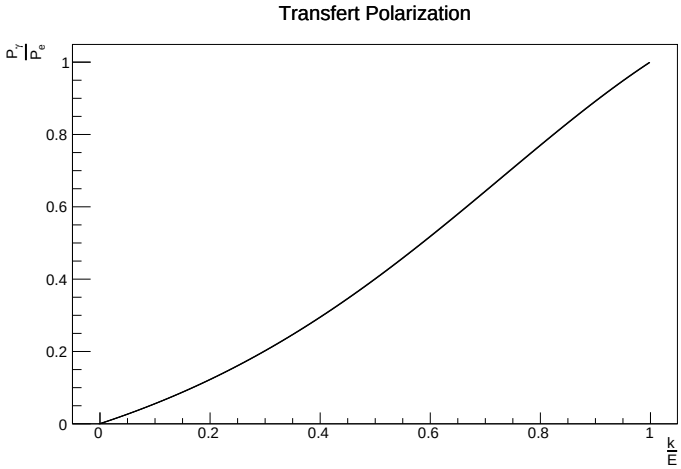

Figure 4: Polarization transfer during the bremsstrahlung interaction.

A Compton transmission polarimeter measures the polarization of an incident beam of electrons through the absorption of polarized photons. In that respect, the key process is the conversion of the incident beam into photons. During this conversion, the polarization state of the primary and created particles change in such a way that part of the beam polarization is transferred to the bremsstrahlung produced photon radiation. Circularly polarized photons are produced when a polarized electron beam strikes a target. The efficiency of the polarization transfer depends on the energy and angle of the emitted photon as well as the energy of the electron. In the forward angle limit [7], it can be written as

$$P_\gamma/P_e = \frac{k}{E}\,\frac{1+\frac{1}{3}\left(1-\frac{k}{E}\right)}{1-\frac{2}{3}\left(1-\frac{k}{E}\right)+\left(1-\frac{k}{E}\right)^2} \tag{12}$$

where P_γ is the circular polarization of photons, P_e is the longitudinal polarization component of electrons and E is the kinetic energy of the electron beam. Consequently, the polarization spectra of photons is a continuum in energy up to the polarization of initial electrons (Fig. 4).

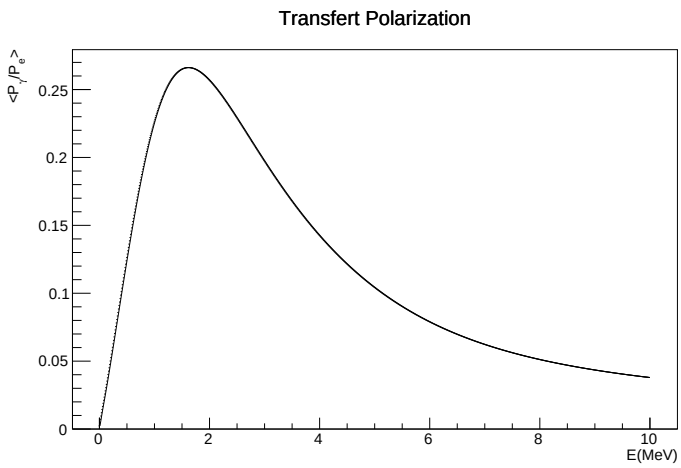

Figure 5: Average polarization transfer during bremsstrahlung interaction.

A more global characterization of the polarization transfer can be obtained from the convolution of the polarization transfer efficiency with the energy dependence of the bremsstrahlung spectra. This can

be expressed in the average polarization transfer

$$\langle P_\gamma / P_e \rangle = \int_{k_{th}}^{E-m} dk \, \frac{d\sigma}{dk} \, \frac{P_\gamma}{P_e} \Big/ \int_{k_{th}}^{E-m} dk \, \frac{d\sigma}{dk} \tag{13}$$

where k_{th} is a photon energy threshold which can be interpreted as the minimum photon energy to generate an interaction with significant energy release, similar in effect to GEANT4 reaction thresholds. The sensitivity of the average polarization transfer to the electron beam energy is shown in Fig. 5. In this simple single-interaction approach, Compton transmission polarimetry appears most appropriate for low energy electrons (< 5 MeV). However, this represents only a rough approximation since an electromagnetic shower is the complex sum of many single interactions.

3 Compton transmission polarimetry and modeling

3.1 Principle of operation

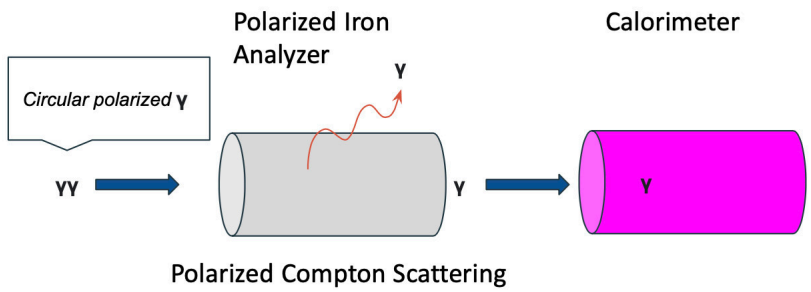

Figure 6: Schematic of the analyzer and the calorimeter parts of a Compton transmission polarimeter.

The polarization sensitive part of a Compton transmission polarimeter can be restricted to the absorption of a photon beam by a polarized material (Fig. 6). While photons interact with matter according to different physical processes, only Compton scattering is - for sake of simplicity - considered in the following. Assuming mono-energetic photons, the probability transfer of a photon, that is the probability for no interaction with the electrons of the analyzer, is described by the exponential law

$$\varepsilon_T^{\pm}(L) = \exp[-(\mu_0 \pm P_\gamma P_t \mu_1) L] \tag{14}$$

where P_t is the polarization of the analyzer electrons and the upper signs indicate the orientation of the circular polarization of photons. μ_0 and μ_1 are the Compton attenuation coefficients defined as

$$\mu_0 \equiv \mu_0(k) = \rho_e \int d\theta d\phi \, \frac{d^2\sigma_C^0}{d\theta\phi} \tag{15}$$

$$\mu_1 \equiv \mu_1(k) = \rho_e \int d\theta d\phi \, \frac{d^2\sigma_C^0}{d\theta\phi} \, A_3(\theta) \tag{16}$$

where ρ_e is the electronic density of the analyzer, L is its length, and $d^2\sigma 0_C / d\theta\phi$ is the unpolarized Compton scattering cross section defined in Eq. (6).

$$A_3(\theta) = \left[\frac{k_0}{k} - \frac{k}{k_0} \right] \cos(\theta) \Big/ \frac{k_0}{k} + \frac{k}{k_0} - \sin^2(\theta) \tag{17}$$

is the analyzing power of the Compton scattering process, that is somehow the polarization efficiency of the process which happens to be energy and angle dependent.

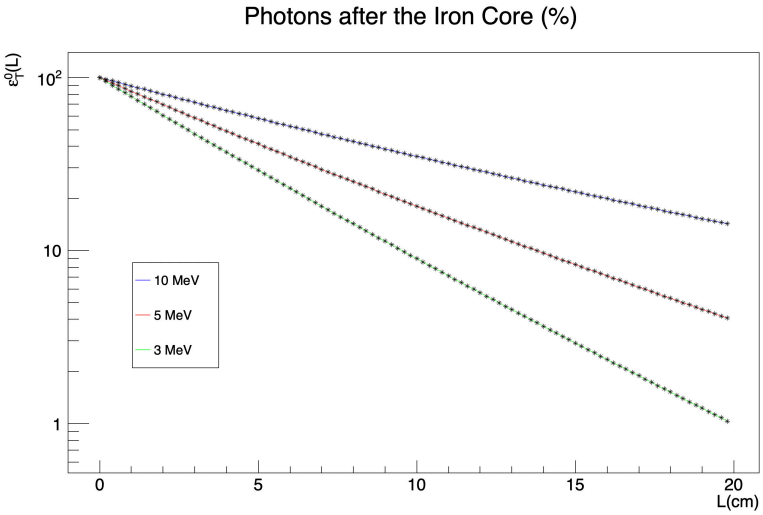

Figure 7: Transmission efficiency of mono-energetic photons in iron.

Considering the numbers $N_\gamma^+ = N_\gamma^- = N_0$ of initial photons, the total number of transmitted photons defines the transmission efficiency of the polarimeter as the average of right and left circular transmitted photons following the expression

$$\varepsilon_T^0(L) = \frac{N_\gamma^+ \varepsilon_T^+(L) + N_\gamma^- \varepsilon_T^-(L)}{N_\gamma^+ + N_\gamma^-} = \exp\left(-\mu_0 L\right) \cosh(P_\gamma P_t \, \mu_1 L)\,, \tag{18}$$

where the polarization sensitive part is generally well approximated by 1. Using Eq. (15) and Eq. (16), and assuming $P_\gamma = \pm 1$ and $P_t = 1$ (note that for an iron analyzer sitting at the core of a magnet, the maximum analyzer polarization is 0.08), the attenuation coefficients have been determined for different photon energies via a numerical integration based on a trapezoidal method. The corresponding transmission efficiency is represented in Fig. 7 for different photon energies as function of the analyzer length. At a given length, high energy photons are more easily transmitted because of a smaller Compton cross section.

Comparing the number of transmitted photons, the photon count asymmetry defines the experimental asymmetry $A_m(L)$ as

$$A_m(L) = \frac{N_\gamma^+ \varepsilon_T^+(L) - N_\gamma^- \varepsilon_T^-(L)}{N_\gamma^+ + N_\gamma^-} = \tanh(-P_\gamma P_t \, \mu_1 L)\,. \tag{19}$$

For $|P_\gamma| = 1$ and $P_t = 1$, this quantity represents the counting anlayzing power $\delta_\gamma(L)$ of the polarimeter which can be interpreted as the polarimeter capability for measuring the polarization of photons. In that case, the analyzer reveals the polarization of the incident beam from the asymmetry of the photon count. It should be noted that this asymmetry does not depend on the linear attenuation coefficient μ_0 but only on the polarization sensitive attenuation coefficient μ_1. The photon energy dependence of the analyzing power is represented on Fig. 8. Low photon energies supports higher analyzing power resulting in a greater gap between polarized populations.

Eq. 19 further shows, that for a realistic iron analyzer, the asymmetry is essentially linearly proportional to the photon polarization. Consequently, for a polarimeter of known length and a photon beam of known energy, the photon polarization can be expressed as

$$P_\gamma = \frac{A_m(L)}{P_t \, \delta_\gamma(L)}\,. \tag{20}$$

The statistical uncertainty on this measurement writes

$$\delta P_\gamma = \left[2 N_0 \, P_t^2 \, \epsilon_T^0(L) \delta_\gamma^2(L)\right]^{-\frac{1}{2}} = \left[2 N_0 \, P_t^2 \, \mathrm{FoM}\right]^{-\frac{1}{2}} \tag{21}$$

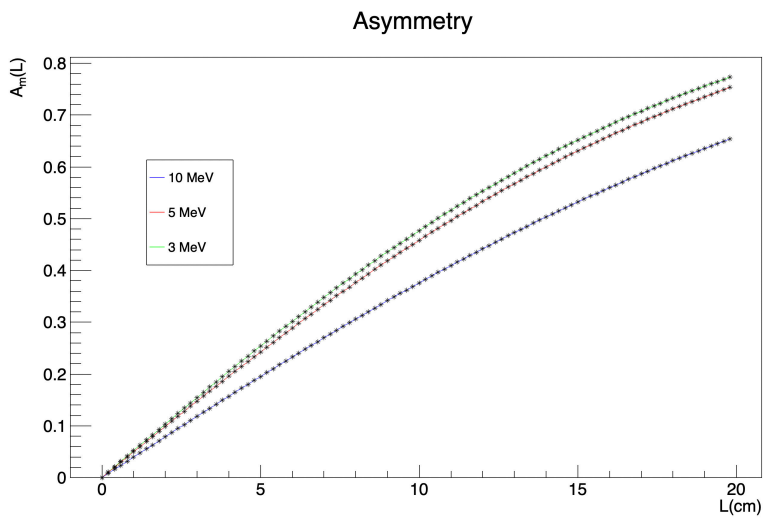

Figure 8: Counting analyzing power of mono-energetic photons in iron.

which defines the Figure-of-Merit (FoM) of the polarimeter as the product of the transmission efficiency and of the square of the analyzing power. While the analyzing power increases with the analyzer length and the transmission efficiency decreases with L, the FoM combines these two features in one single parameter which optimum value ensures an optimum uncertainty. The FoM is then the parameter of interest for an optimization of the performance of a polarimeter.

3.2 Extension to an electron beam

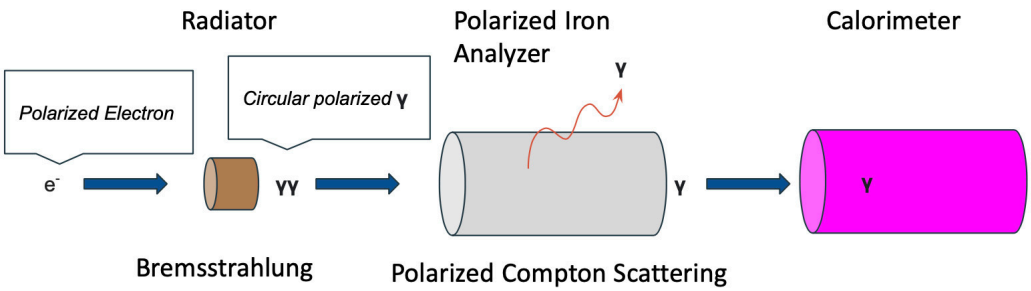

Figure 9: Schematic of the full Compton tranmission polarimeter.

The use of a Compton transmission polarimeter to measure the polarization of an electron beam implies the transformation of the incident polarized electrons into circularly polarized photons. This is achieved with a radiator where electrons convert into photons through the bremsstrahlung process. The radiator configuration can also be part of the optimization procedure. However, in the final experimental context, this radiator is assumed to be part of a water-cooled beam dump which purpose is to stop incident electrons. The radiator is so optimized for electron absorption and not polarized photon production and measurement. It is actually expected to be made of a 7 mm thick piece of copper.

In an attempt to predict the relative variation of the polarimeter performance, the transmission efficiency and analyzing power should take into account the initial bremsstrahlung distribution of polarized photons. The polarimeter performances can then be expressed as an average response weighted by the bremsstrahlung cross section. Similarly to the average polarization transfer (Eq. (13)), the average

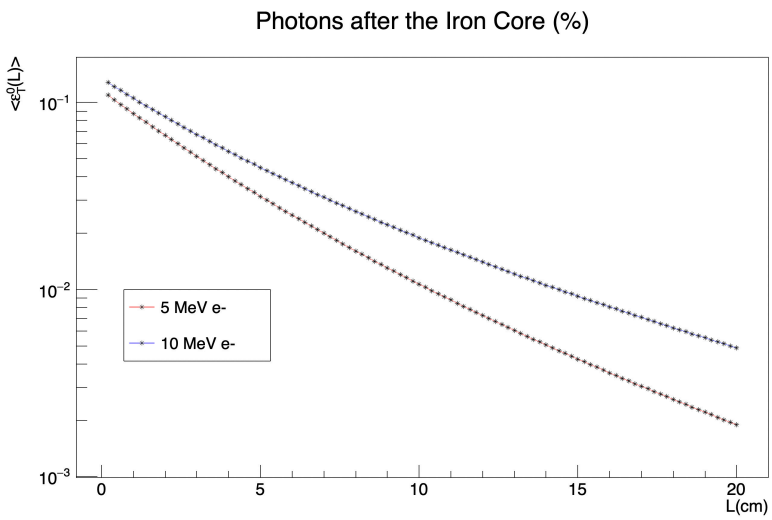

Figure 10: Transmission efficiency of the polarimeter for mono-energetic electrons.

transmission efficiency for each helicity state ($\pm$) of the electron beam can be written

$$\langle \varepsilon_T^{\pm}(L) \rangle = \int_{k_{th}}^{E-m} dk \exp\left[-\mu^{\pm}(k)L\right] \frac{d\sigma}{dk} \Big/ \int_{k_{th}}^{E-m} dk \, \frac{d\sigma}{dk} \tag{22}$$

where $d\sigma/dk$ is the bremsstrahlung cross section defined in Eq. (1), and $\mu(k)$ is the linear attenuation coefficient of copper defined as

$$\mu^{\pm}(k) = \mu_{\gamma e}(k) + \mu_{e^+e^-} + \mu_0(k) \pm P_e P_t \frac{P_\gamma(k)}{P_e} \, \mu_1(k) \tag{23}$$

where all the relevant photon absorption processes have been considered. Assuming the same number of incident electrons per helicity state ($N_e^+ = N_e^- = N_e$), the unpolarized average transmission efficiency is defined according to

$$\langle \varepsilon_T^0(L) \rangle = \frac{N_e^+ \langle \varepsilon_T^+(L) \rangle + N_e^- \langle \varepsilon_T^-(L) \rangle}{N_e^+ + N_e^-} = \frac{\langle \varepsilon_T^+(L) \rangle + \langle \varepsilon_T^-(L) \rangle}{2} \, , \tag{24}$$

and the corresponding count asymmetry writes

$$\langle A_m(L) \rangle = \frac{N_e^+ \langle \varepsilon_T^+(L) \rangle - N_e^- \langle \varepsilon_T^-(L) \rangle}{N_e^+ \langle \varepsilon_T^+(L) \rangle + N_e^- \langle \varepsilon_T^-(L) \rangle} = \frac{\langle \varepsilon_T^+(L) \rangle - \langle \varepsilon_T^-(L) \rangle}{\langle \varepsilon_T^+(L) \rangle + \langle \varepsilon_T^-(L) \rangle} \, . \tag{25}$$

The sensitivity of these quantities to the analyzer length are represented in Fig. 10-11. The transmission efficiency difference between 5 MeV and 10 MeV electrons turns out to be less significant than in the case of mono-energetic photons. This is a consequence of the bremsstrahlung cross sections which favors the production of low energy photons, and leads to lower transmission efficiencies at higher electron beam energies. The count asymmetry is sensitive to the polarization of the incident beam through the bremsstrahlung induced photon polarization. The sensitivity of the count asymmetry to the electron energy is similar to the mono-energetic photon case: lower beam energies feature larger asymmetries. Because of low energy photons in the bremsstrahlung distribution, electron asymmetries are smaller than photon asymmetries at the same beam energy.

Alternatively, a photon energy asymmetry can also be defined following the expression

$$\langle A_m^E(L) \rangle = \frac{N_e^+ \langle E_T^+(L) \rangle - N_e^- \langle E_T^-(L) \rangle}{N_e^+ \langle E_T^+(L) \rangle + N_e^- \langle E_T^-(L) \rangle} \tag{26}$$

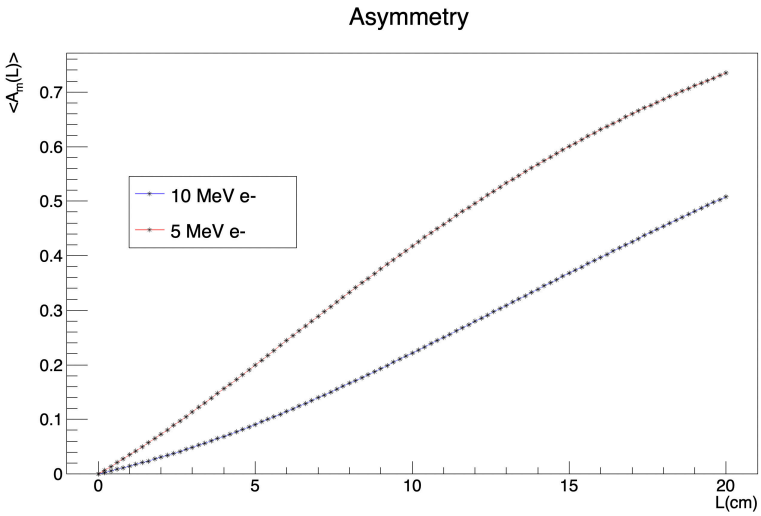

Figure 11: Count asymmetry of the polarimeter for mono-energetic electrons.

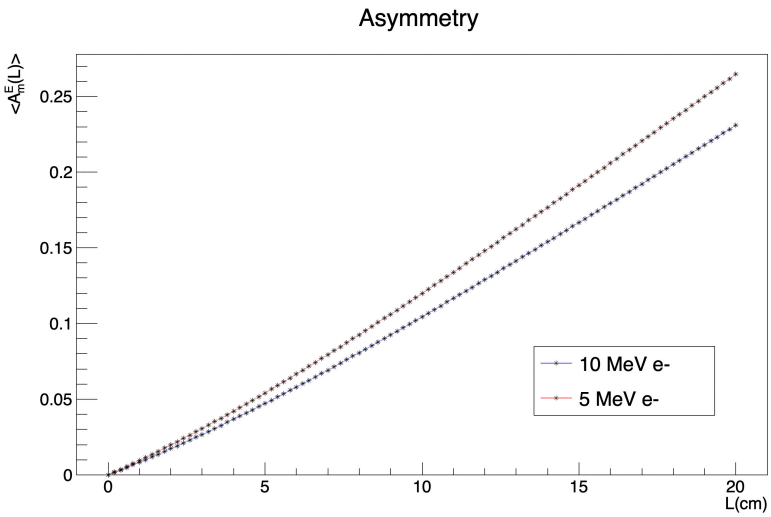

Figure 12: Energy asymmetry of the polarimeter for mono-energetic electrons.

with

$$\langle E_T^{\pm}(L)\rangle = \int_{k_{th}}^{E-m} dk \exp\left[-\mu^{\pm}(k)L\right] k \frac{d\sigma}{dk} \Big/ \int_{k_{th}}^{E-m} dk \, \frac{d\sigma}{dk} \tag{27}$$

which tends to improve the sensitivity to high energy photons where polarization effects are the most significant. The sensitivity of this asymmetry to the analyzer length is shown in Fig. 12. It is remarkable to notice that the energy asymmetry is much less sensitive than the count asymmetry to the initial beam energy.

3.3 Measurement of an electron beam polarization

When the rate of detected events becomes too high to allow for an event-by-event operation, an integrated approach is often chosen which provides an intensity signal directly proportional the population of initial particles. In the present context, this information is obtained from the total energy deposited in the crystal over a period of time (a bunch) where the helicity state of the initial beam and the orientation

of the analyzer polarization do not change. By changing the orientation of the polarization of the laser-light at the photocathode for each bunch, the helicity state of the beam is reversed and an asymmetry is measured in the polarimeter for each bunch pair.

Following previous sections, the response of the Compton transmission polarimeter is sensitive to a certain average polarization of the photons, which is in turn proportional to the initial polarization of the electrons. Experimentally, the calorimeter recovers the energy from the photons, and the measured asymmetry can be expressed from the energy deposit as

$$A_m = \frac{\mathcal{E}_+^+ - \mathcal{E}_+^-}{\mathcal{E}_+^+ + \mathcal{E}_+^-} = \frac{\mathcal{E}_+^+ - \mathcal{E}_-^+}{\mathcal{E}_+^+ + \mathcal{E}_-^+} \tag{28}$$

where the upper signs denotes the helicity state of the beam and the lower ones represents the relative orientation of the target polarization with respect to the electron beam helicity. Particularly, Eq. 28 indicates that the asymmetry can be measured either by reversing the beam helicity or the analyzer polarization. This is of specific interest to search and correct for false asymmetries [8]. Considering the helicity reversal case, the energy deposit per helicity state can be written

$$\mathcal{E}^{\pm} = N_e^{\pm} \sum_i \varepsilon_0^i \left(1 \pm P_e P_t \, A_i^e\right) E_i \tag{29}$$

where the sum runs over the full range of photon energies detected in the calorimeter; $N_e^{\pm}$ is the total number of electrons per helicity state, ε_0^i is the unpolarized efficiency that is the probability for releasing the energy E_i in the calorimeter from an electron, and A_i^e is the global analyzing power of the polarimeter for a given electron beam releasing the energy E_i in the calorimeter. This latter quantity can be obtained from calibration measurements using a beam of known polarization, or from the simulation of the response of the full polarimeter. Assuming $N_e^+ = N_e^- = N_e$, the experimental asymmetry becomes

$$A_m = P_e P_t \sum_i \varepsilon_0^i A_i^e E_i \Big/ \sum_i \varepsilon_0^i E_i = P_e P_t \, \frac{\langle A^e E \rangle}{\langle E \rangle} \tag{30}$$

with

$$\langle A^e E \rangle = \sum_i \varepsilon_0^i A_i^e E_i \Big/ \sum_i \varepsilon_0^i = \sum_i \varepsilon_0^i A_i^e E_i \Big/ \varepsilon_0 \tag{31}$$

$$\langle E \rangle = \sum_i \varepsilon_0^i E_i \Big/ \varepsilon_0 \, . \tag{32}$$

The statistical uncertainty on this asymmetry originates from the statistical distribution of the number of detected photons with a given energy E_i. In the case of small experimental asymmetries, it can be expressed as

$$\left(\delta A_m\right)^2 = \frac{1}{2\varepsilon_0 N_e} \frac{\langle E^2 \rangle}{\langle E \rangle^2} \, . \tag{33}$$

For each bunch pair j, the electron beam polarization can be inferred according to

$$P_e^j = \frac{1}{P_t} \frac{\langle E \rangle}{\langle A^e E \rangle} \, A_m^j \, . \tag{34}$$

The final polarization value is then expressed as an average over the total number N_b of bunch pairs according to

$$P_e = \frac{1}{N_b} \sum_{j=1}^{N_b} P_e^j \, . \tag{35}$$

Correspondingly, the statistical uncertainty on the measured polarization can be written as

$$\delta P_e = \left[2\varepsilon_0 N_b N_e P_t^2 \, \frac{\langle A^e E \rangle^2}{\langle E^2 \rangle} \right]^{-\frac{1}{2}} = \left[2 N_b N_e P_t^2 \, \mathrm{FoM} \right]^{-\frac{1}{2}} \tag{36}$$

which, similarly to Eq. (21) defines the Figure-of-Merit of the polarimeter for electrons. The energy range of interest in this study extends over the 5-10 MeV range, in accordance with available energies at the CEBAF injector as well as the possibility of cross-calibration with respect to the existing Mott polarimeter.

4 Optimization of the polarimeter components

4.1 The GEANT4 framework

The GEANT4 software [9] was developed at CERN and uses the Monte-Carlo method to evaluate, among others, the response of a detector. To operate a simulation, it is necessary to define the global context and specific aspects of the study following the main items `Geometry` : choosing the geometry and materials of what is to be simulated.
`Physics list` : defining the particles as well as the physical phenomena that will be taken during the simulation.
`Primary generator` : choosing the characteristics of the incident particle beam, including its energy and polarization.
`Run action` : initializing histograms and the Ntuples that will be filled during each event, as well as the number of incident particles; over a run, none of these aspects can be changed.
`Event action` : filling histograms and the Ntuples of selected data; for example, during our simulation, an event corresponds to an electron of the incident beam, and the energy deposited in the crystal is recorded for each electron.
`Stepping action` : over the course of an event, calculations are done in steps, corresponding to the lowest simulation scale; at each step, the kinetic energy, the time, and the polarization state of a particle can be recorded.

4.2 Optimization of the calorimeter

The goal of the present study is the optimization of the size of a calorimeter detector intended to measure the energy of incident photons. The Molière radius as well as the radiation length of a material are both giving an idea of response of a crystal with respect to its dimensions: the Molière radius is defined as the radius of a cylinder containing at least 90% of the energy deposited by an electromagnetic shower developping within a material; the radiation length corresponds to the average distance necessary to reduce the energy of an incoming electron by a factor larger than $1/e$. For a BGO crystal, the Molière radius is 2.3 cm and the radiation length is 1.1 cm.

4.2.1 BGO radius and length optimization

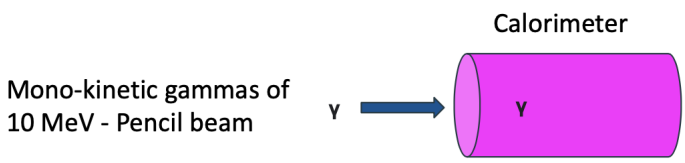

Figure 13: Calorimeter modeling within GEANT4.

The purpose of the calorimeter is to recover the energy of the incident photons. The initial choice of BGO material is motivated by the actual availability of in-house crystals with dimensions: L=15 cm, R=2.5 − 3.5 cm). The study then focuses on the amount of energy collected by a crystal for mono-energetic photons. The evolution of the efficiency of the energy deposit, defined as

$$\varepsilon_D = \frac{< E_{BGO} >}{E_\gamma}\,, \tag{37}$$

is determined for different crystal sizes. In this expression, $< E_{BGO} >$ is the average energy deposit for an initial photon population, numerous enough to ensure an accurate determination of ε_D.

The calorimeter is modeled within GEANT4 by a cylinder illuminated with a pencil-beam of mono-kinetic photons impinging at its center (Fig. 13). A *phantom* detector surrounding all the active volume

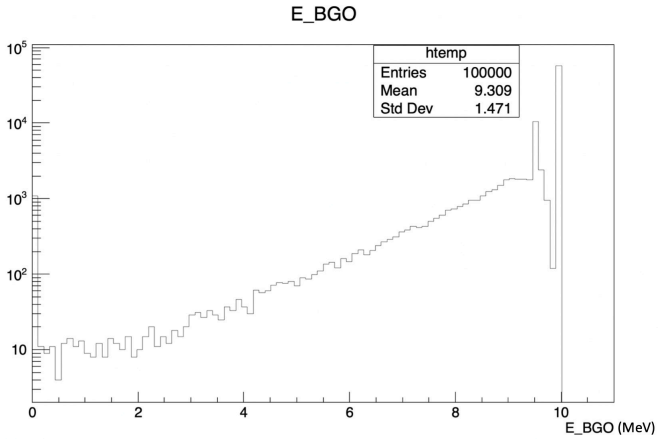

Figure 14: Energy deposit spectrum of 10 MeV photons in a BGO crystal (L, R)=$(15, 3.5)$ cm.

of the crystal has been added to obtain information about the origin of eventual energy leakages. A total number of 10^5 photons is sent for each size configuration, and the energy deposit is recorded in an histogram. The spectrum in Fig. 14 is typical of the crystal response to γ-radiations. The photons can interact through photo-electric, Compton or pair-creation processes. They can experience several Compton scattering before releasing energy through photo-electric or pair creation effects: a continuous spectrum until the retro-diffusion peak at 9.75 MeV is observed, followed by the total absorption peak at the incident photon energy, here 10 MeV.

The analysis of the crystal radius simulations is reported on Fig. 15. From the Molière's radius, we expect to recover 90% of the energy of the incident photon for a 2.3 cm radius. Indeed, a somehow universal saturation behaviour is observed which is reached at about 3.0 cm. However, it should be noted that the saturation level depends on the crystal length. For too short a length, a significant amount of the energy is lost in the forward direction. With increasing length, part of this energy is recovered and the saturation level reaches larger values. For too short a radius, it can be noted that lateral leaks become very significant. In such cases, the calorimeter recovers only a small part of the incident beam. Because of the multiple Compton interactions, the energy leaks outside the crystal from the sides. Similarly, the analysis of the crystal length simulations is reported on Fig. 16. Accordingly, the combination (L, R)=$(15, 3.5)$ cm allows to recover 90% of the energy of the incident beam. As expected from the radiation length, we observe that the forward leaks become very significant for short crystal lengths. Analogously to the previous observation, the saturation level depends on the crystal radius.

The complete mapping of the efficiency of the energy collection of the crystal is represented on Fig. 17 for a large range of length and radius. Defining an efficiency threshold at 95%, one can extract optimum length and radius to operate a crystal with 10 MeV photons, for instance a minimum length of 18 cm for a 3.5 cm radius. For comparison, the available crystals in-house have an efficiency about 91% and 93.78 for respectively 2.5 cm and 3.5 cm radii, that are below the selected threshold.

4.2.2 Influence of the photon energy

The study was conducted for a mono-energetic photon beam at the highest energy available at the CEBAF injector. However, the radiator of the polarimeter will cause a distribution of the energy of the photons (Fig. 2), and one has to ensure that a crystal optimized at 10 MeV still delivers an optimal response at smaller energies. As a source of comparison, the same simulation protocol was carried out for 5 MeV photons (Fig. 18). For long enough crystal, the general trend when reducing the initial energy is an increase of the transverse size of the shower, which requires larger radius crystals: for a 18 cm long crystal, we observe an increase of 0.3 cm in the radius corresponding to the same energy collection efficiency. These effects are consistent with the Lorentz boost of shower particles from initial photons, and remains small enough for our purposes. An appropriate strategy is then to optimize the radius with respect to the most probable photon energies, and the length with respect to the highest energies.

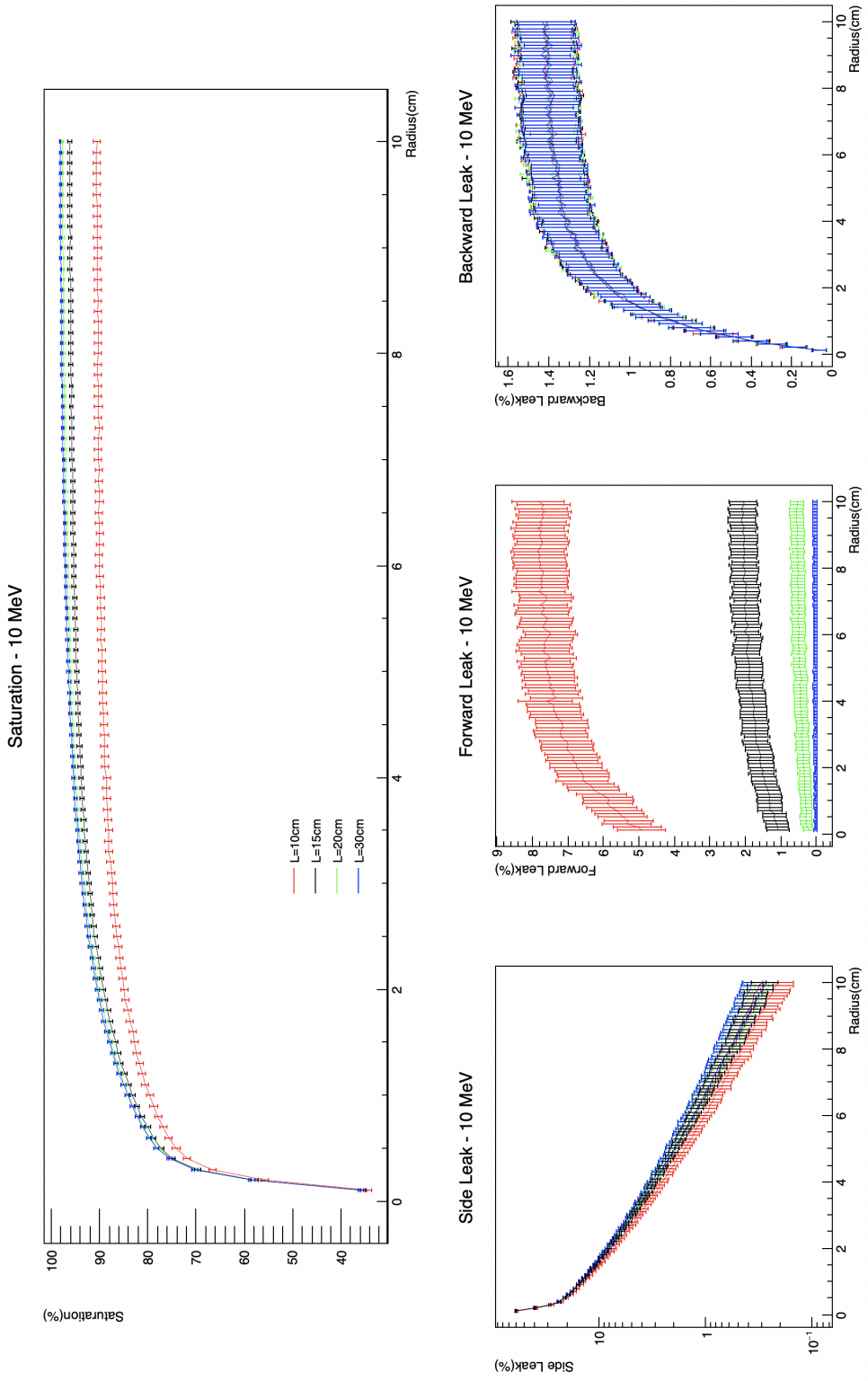

Figure 15: Optimization of the crystal radius for 10 MeV photons.

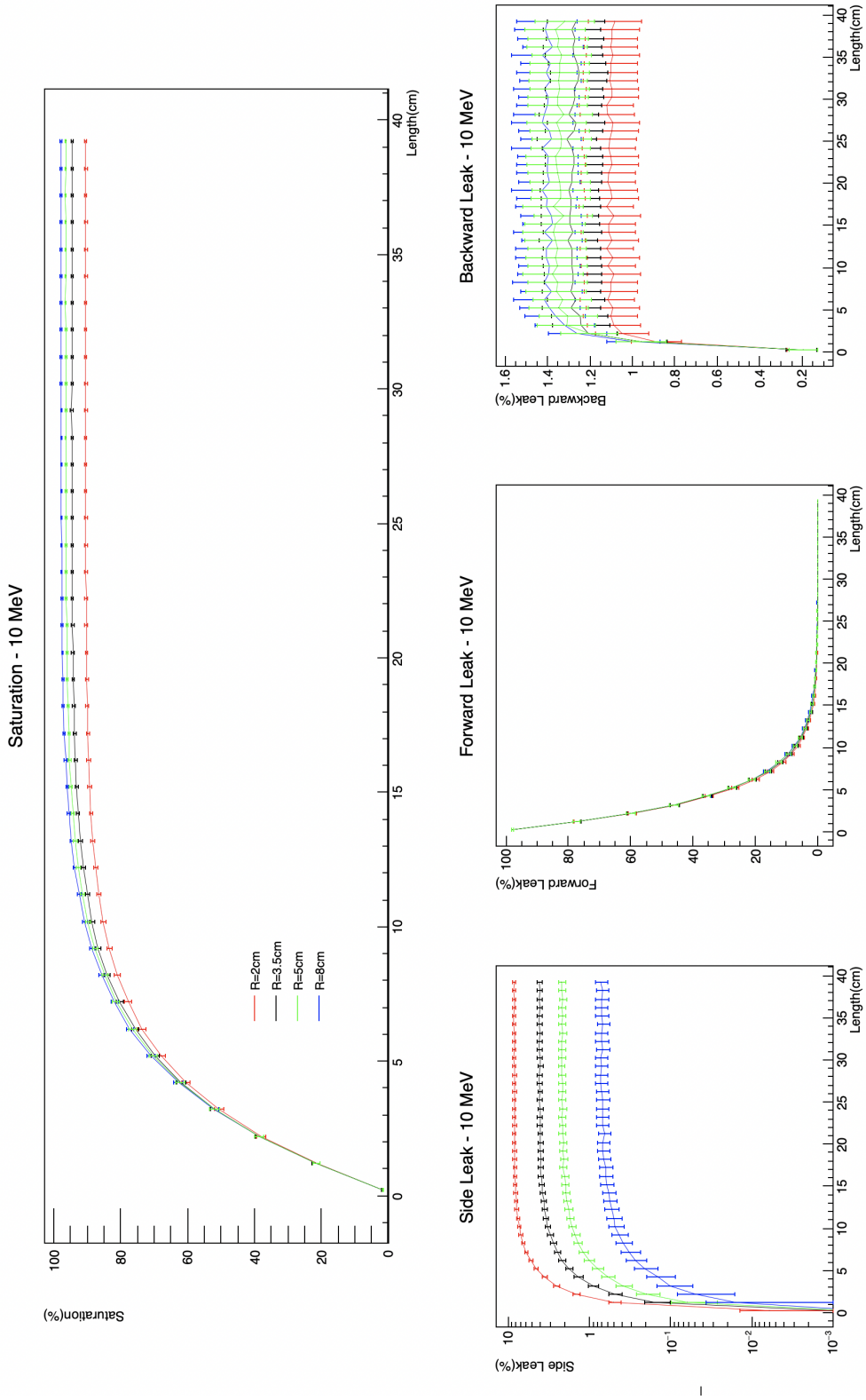

Figure 16: Optimization of the crystal length for 10 MeV photons.

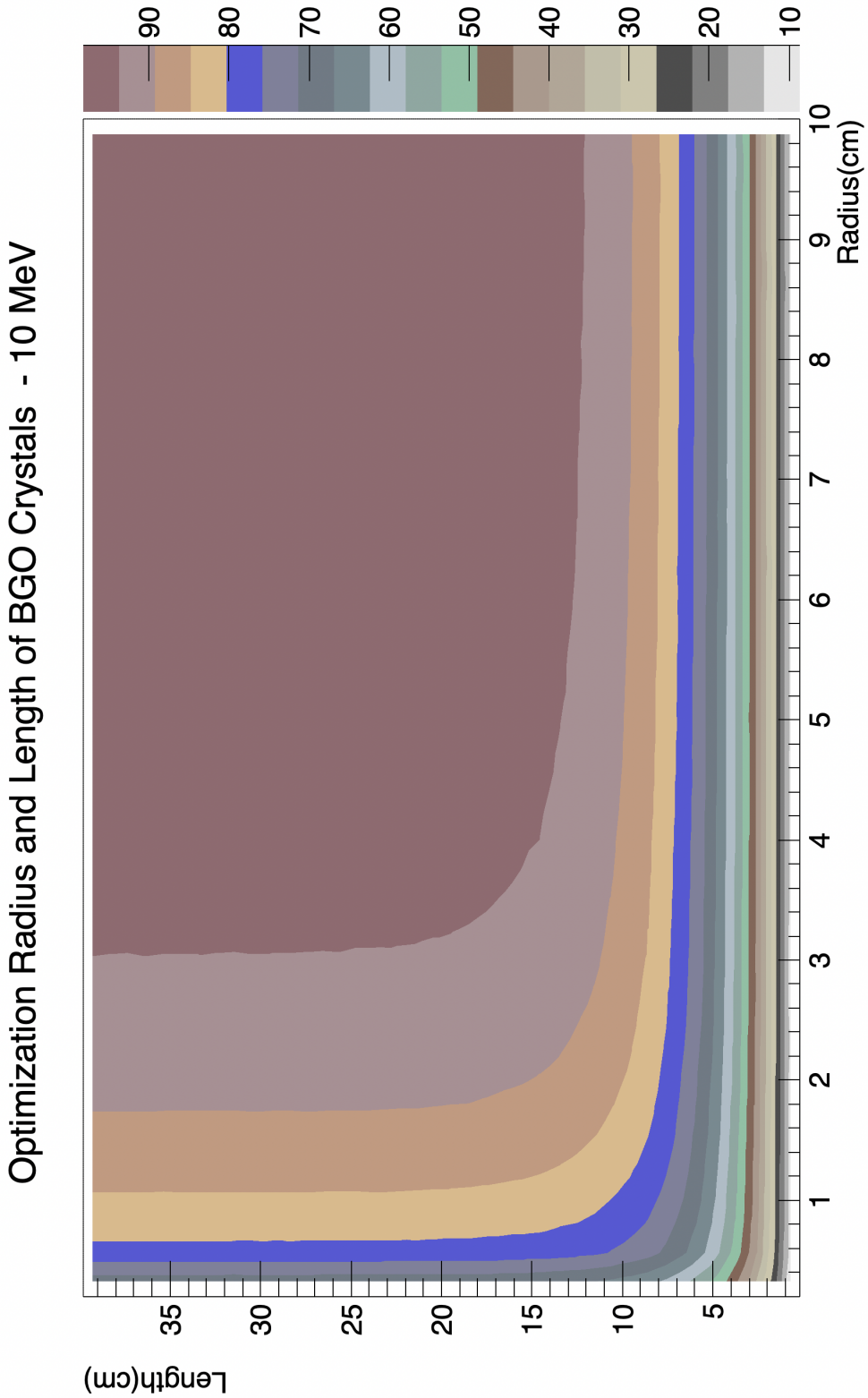

Figure 17: Mapping of the efficiency of the energy collection of a BGO crystal for 10 MeV photons.

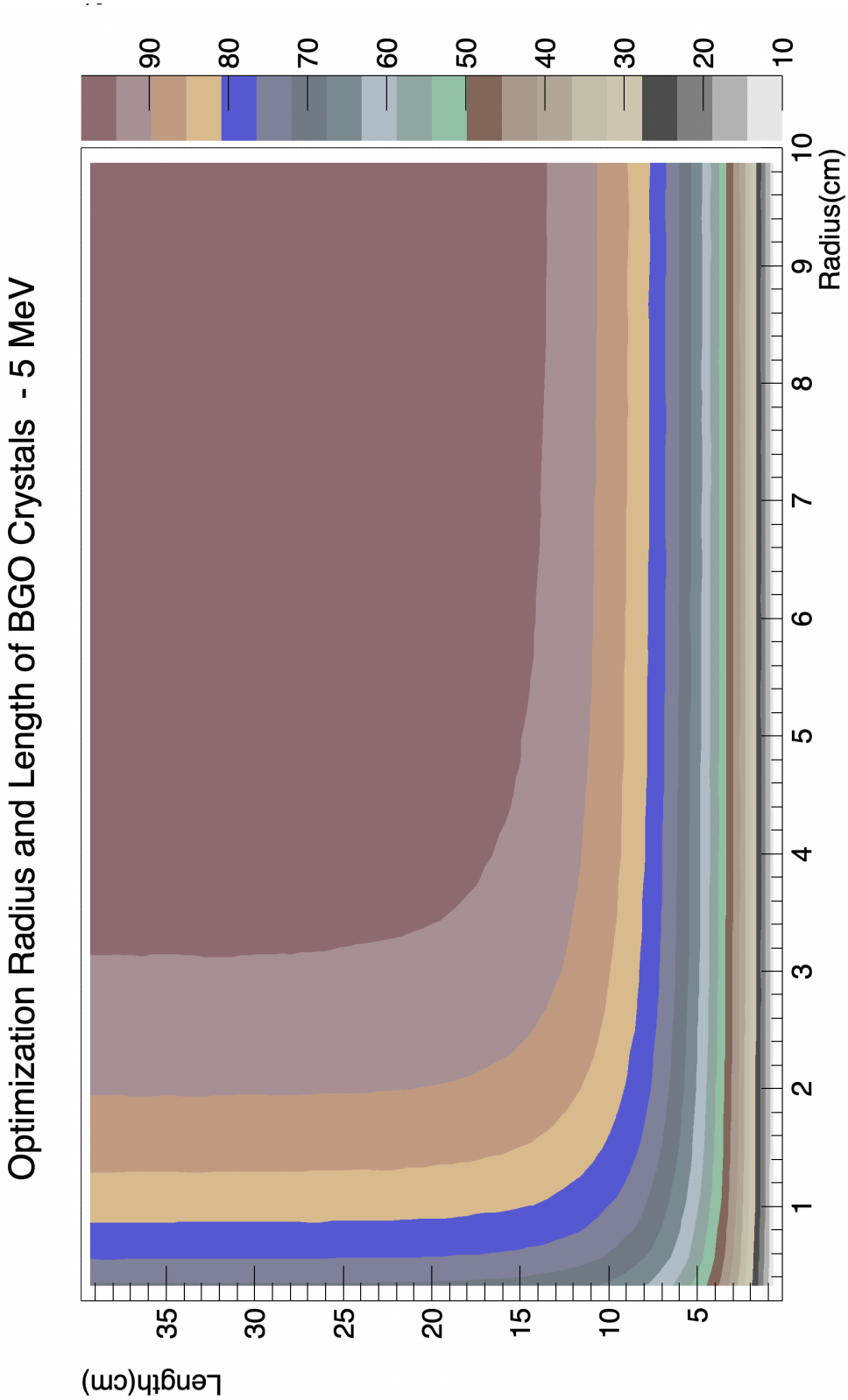

Figure 18: Mapping of the efficiency of the energy collection of a BGO crystal for 5 MeV photons.

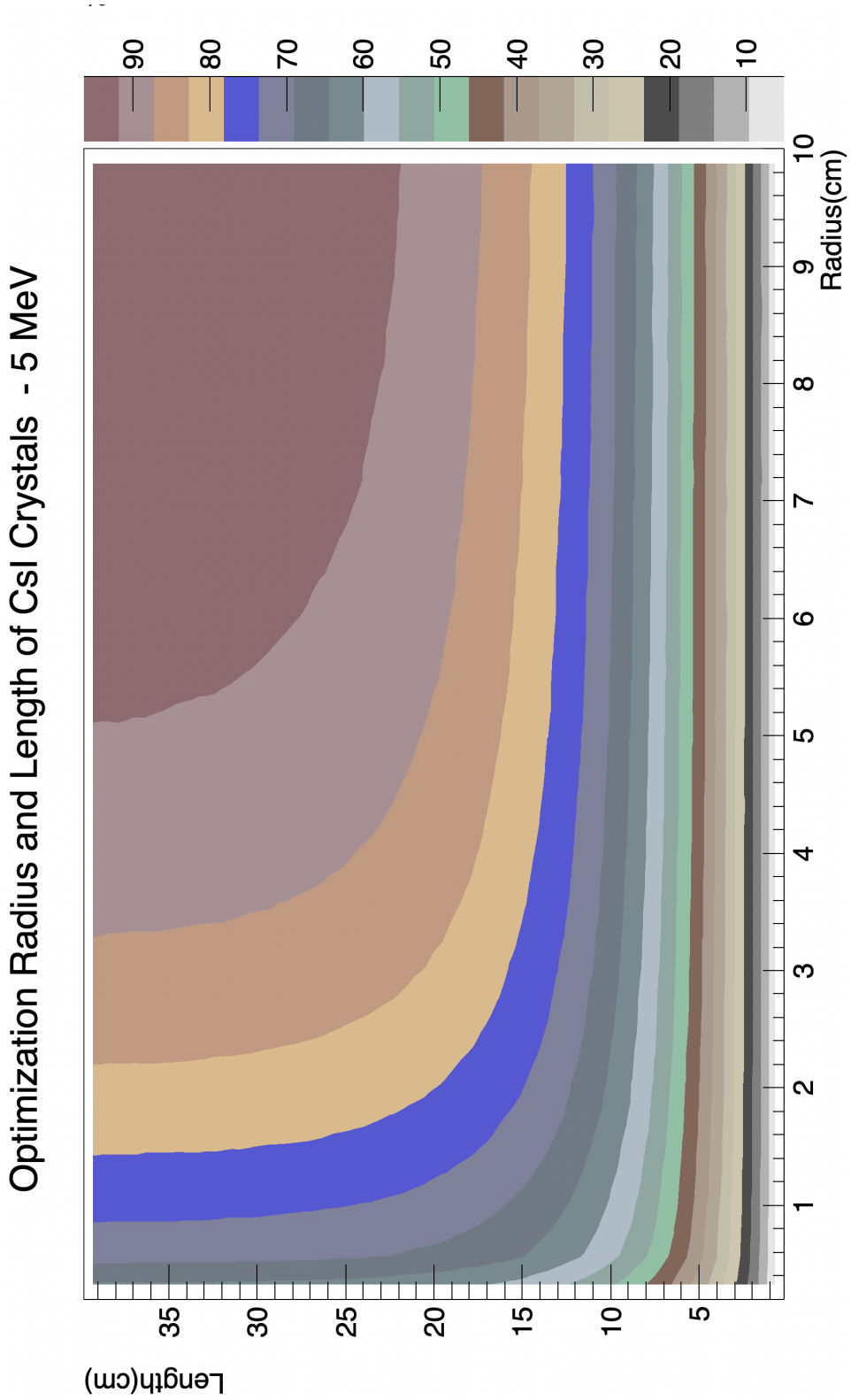

Figure 19: Mapping of the efficiency of the energy collection of a CsI(Tl) crystal for 5 MeV photons.

4.2.3 Influence of the crystal material

There exists different types of calorimeter crystals regarding the energy range of initial particles, the light yield efficiency... The PEPPo experiment, operating a similar polarimeter, was using CsI(Tl) - thallium-doped cesium iodide - crystals which properties differ from BGO ones (Tab. 1). In particular, the Molière radius and the radiation length of CsI(Tl) crystals are larger than BGO's, anticipating larger sizes for similar energy collection efficiencies. The simulation protocol for CsI(Tl) was carried out at 5 MeV photons (Fig. 19). For a (L, R)=$(15, 3.5)$ cm crystal, the CsI(Tl) collects 78% of the incident beam energy while the BGO reaches 92%. In that volume/efficiency respect, the BGO is a much better candidate. A more technical aspect concerns the decay time of the signal delivered by the crystal: BGO crystals are faster and more adapted to the constraints of the data acquisition systems which deals with 1 μs time windows. BGO crystals are then favored for the present Compton transmission polarimeter.

Material	Molière radius (cm)	Radiation length (cm)	Decay time (ns)
CsI(Tl)	3.53	1.86	630
$Bi_4Ge_3O_{12}$	2.26	1.12	300

Table 1: Physical properties of BGO and CsI(Tl) crystals.

4.3 Optimization of the analyzer

In order to optimize the analyzer, we simulate the entire Compton transmission polarimeter (Fig. 20). The radiator is made out of copper to optimize the bremsstrahlung radiation rate and to allow easy cooling implementation. We remind that the objective is to convert the incident electrons into photons, so we aim a radiator acting as a dump for electrons. Furthermore, it is important to note that photons are no longer mono-energetic, such that the relevant formalism of the polarization measurement is the one presented in Sec. 3.3.

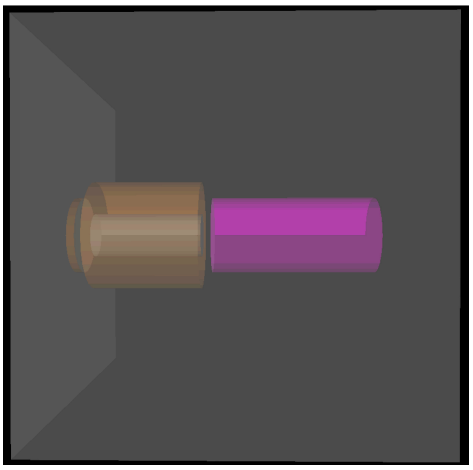

Figure 20: GEANT4 modelling of the polarimeter whch comprises: a copper radiator, an iron surrounded by a copper coil, and a BGO calorimeter.

The thickness of the copper is 7 mm. This parameter is not part of the optimization, and appears as an external constraint for compactness and operation of the apparatus. The simulation protocol involves considering 10×10^6 electrons within a pencil beam configuration impinging at the center of the radiator. To improve the determination of polarization effects, the initial beam polarization P_e and the iron analyzer polarization P_t are set to 1. For each electron, the energy deposit in the crystal is recorded. The number of photons created is like 7 for 1000 electons. Photons are emitted within a wide energy

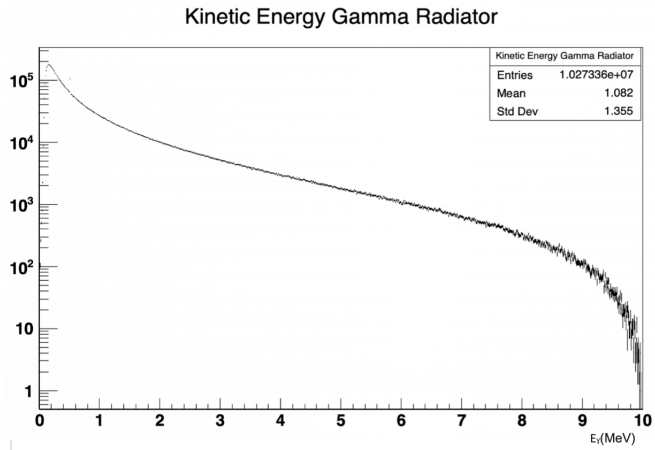

Figure 21: Photon spectrum at the exit of the radiator for 10x10^6 incident electrons of 10 MeV.

distribution as secondary particles resulting from the bremsstrahlung radiation of initial and secondary electrons (Fig. 21). It should be stressed that very few photons with an energy equivalent to the incoming beam energy are produced. The majority of photons have low energies. The purpose of the study is to select an optimized length for the iron analyzer, suitable for operating in the 5-10 MeV energy range. For a better determination of the calorimeter response, a copper coil is added around the analyzer, to simulate the magnet coil that will polarize the electrons of the iron.

4.3.1 Transmission efficiency

The behaviour of the analyzer according to its length needs to be determined. Whenever one or several photons are transmitted from a single initial electrons, the calorimeter signal is recorded. An event with no energy deposit in the calorimeter corresponds to the full absorption of secondary particles before reaching the crystal. On the opposite, an event with a non-zero energy deposit means that the photon has passed through the iron entirely. We then compare $N_\gamma^\pm$ with the number of initial electrons (20×10^6). The efficiency ε_T^0, average over parallel and anti-parallel helicities of the electron is shown on Fig. 22. For example, considering a 8.0 cm long analyzer, the transmission efficiency is 1.74% for 10 MeV primary electrons and 0.62% for 5 MeV.

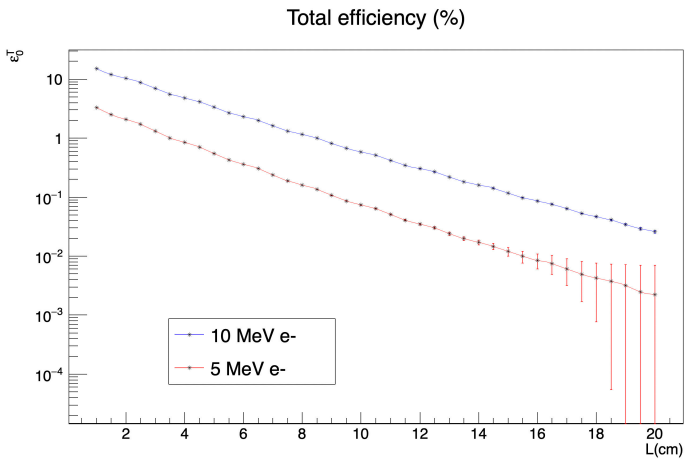

Figure 22: Analyzer length dependence of the helicity average transmission efficiency determined for 20×10^6 pencil-beam electrons.

Simulation are in fair agreement with the rough theorical approach presented in Fig. 10, as far as the relative variation with respect to the analyzer length. The transmission efficiency is higher for 10 MeV than 5 MeV. Assuming a minimum efficiency of 0.1%, Fig. 22 suggests that the iron length should be smaller than 10 cm. This single argument should however be weighted with the iron-length sensitivity of the asymmetry.

4.3.2 Asymmetry

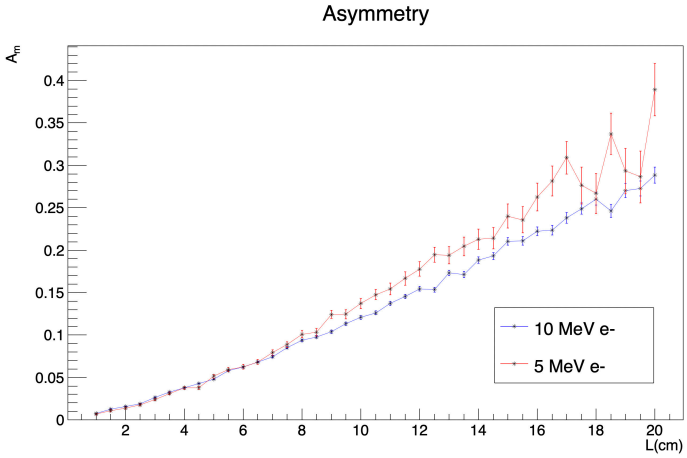

Figure 23: Analyzer length dependence of the experimental asymmetry determined for 20×10^6 pencil-beam electrons and fully polarized beam and analyzer.

We calculate the asymmetry A_m which is previously define in Eq. (28). For each length, the total energy deposit for both electron helicity states (+ or -) state is determined, which corresponds respectively to $\mathcal{E}^+$ and $\mathcal{E}^-$. Once again, simulations are in fair agreement with the single-step theoretical approach (Fig. 12). The asymmetry increases with the length of the analyzer. Actually, the analyzing power of iron analyzer is higher since the number of photons interacting with iron is higher. According to Fig. 23, the asymmetry is maximum for a maximum length. However, at large lengths, the transmission efficiency is too low: the calorimeter does not recover enough photons. It is therefore necessary to consider the Figure-of-Merit to optimize the analyzer length.

4.3.3 Figure of merit

The FoM, defined in Eq. (36), combines the efficiency and asymmetry dependencies to hopefully allow us to conclude on the optimal length of the iron analyzer. It is determined from simulations according to the expression

$$\mathrm{FoM} = \varepsilon_0 \frac{\langle E\rangle^2}{\langle E^2\rangle} \left[A_m(P_e = 1, P_t = 1)\right]^2 = \varepsilon_0 \frac{\langle E\rangle^2}{\langle E^2\rangle} \left[A_m^{11}\right]^2. \tag{38}$$

The Fig. 24 shows the sensitivity of the product $\varepsilon_0 \left[A_m^{11}\right]^2$ to the analyzer length. It exhibits similar behaviour but different magnitude for 5 MeV and 10 MeV electrons. This is most-likely an effect of the bremsstrahlung process which produces huge number of low energy photons in both cases. As expected, it appears a maximum within the 5-10 cm length-region. Further simulations were performed in this length domain with a statistics reaching up to 100×10^6. The corresponding results are shown in Fig. 25. The optimized length of iron, corresponding to the maximum FoM finally turns out to be 8.0 cm.

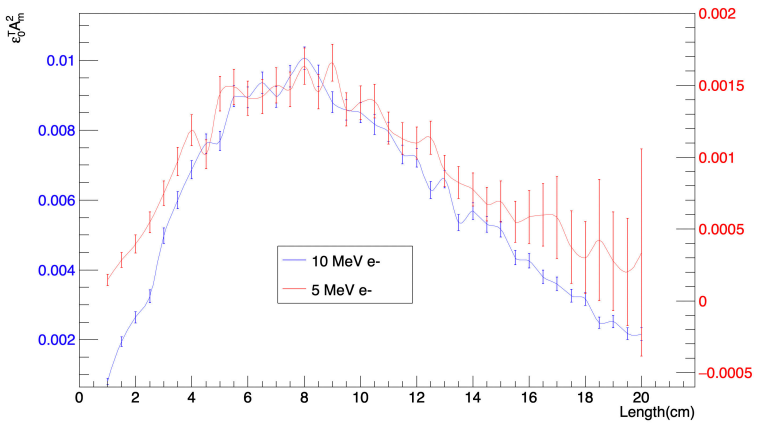

Figure 24: Analyzer length dependence of the reduced FoM determined for 20×10^6 pencil-beam electrons and fully polarized beam and analyzer.

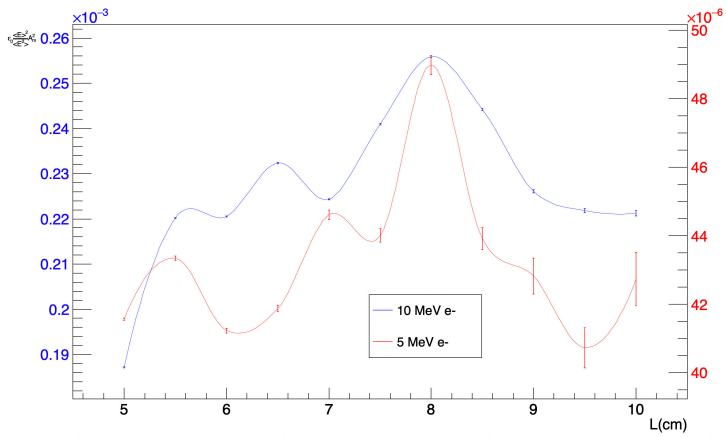

Figure 25: Analyzer length dependence of the FoM determined for 100×10^6 pencil-beam electrons and fully polarized beam and analyzer.

5 Further considerations on the polarimeter operation

5.1 Radiation damage evaluation

Irradiation of scintillating crystals results in a dose-dependent reduction of the light-yield which consequently affects the energy calibration and resolution of the crystals. According to Saint-Gobain, which is one of the company providing crystals, BGO scintillation crystals are susceptible to radiation damage starting at radiation doses between 1 and 10 Gray (102-103 rad). The effect is largely reversible with time or annealing which is a very slow process.

The expected beam currents for the experiment are between 1 nA and 1 μA, with a bunch repetition rate of 78 kHz. We use GEANT4 in order to simulate the energy deposit in the crystal and evaluate the dose received. We send 10×10^6 electrons into the Compton transmission polarimeter and obtain the energy deposit spectra in the crystal (Fig. 26). The effective dose D for 1 bunch at 1 μA is then determined following the expression

$$D = \frac{\text{Energy (J)}}{\text{Mass (kg)}} \,. \tag{39}$$

According to the simulation, the total energy deposited in the crystal is 60 GeV for 10×10^6 electrons. At 1 μA, a single bunch comprises 160×10^6 electrons, corresponding to a total deposit of 960 GeV per

bunch, that is 33.80 nGray with the current crystal geometry. Considering the beam repetition rate, the dose deposited in the crystal would be 2.63 mGray per second. Assuming a 1 Gray limit, the operation of the crystal would thus be limited to 2 mn, which is not sustainable for the experiment. A lower beam current would improve this figures but not in a comfortable way. It is therefore necessary to adjust the polarimeter design to allow for smaller dose exposure. A few solutions may be suggested:

- using doped BGO crystal to increase radiation hardness;
- reducing the number of gammas in the calorimeter (absorber, larger distance between the crystal and the analyzer...).

These are expected to affect the transmission efficiency but not the analyzing power of the polarimeter. As a matter of fact, the FoM will decrease while the analyzer length sensitivity (that is the current optimization procedure) would be preserved.

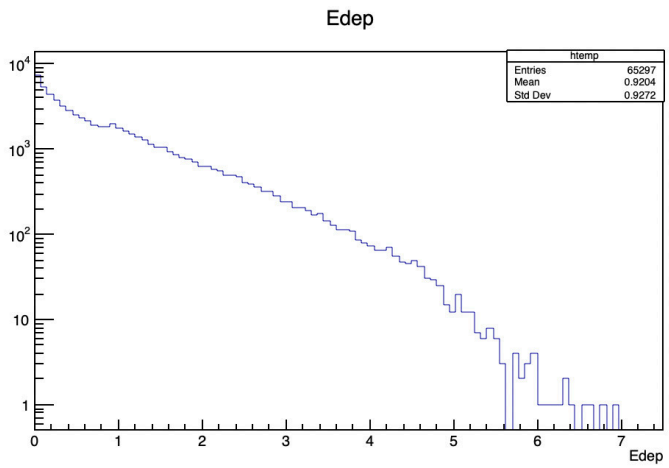

Figure 26: Energy deposit (MeV) in BGO Crystal for 10×10^6 electrons at 10 MeV.

5.2 Duration of a measurement

Following Eq. (36), it is possible to evaluate the duration of a measurement assuming a specific beam polarization and a desired statistical precision. For instance, the total number of electrons N_t required to achieve a measurement with a certain relative uncertainty can be expressed as

$$N_t = 2N_eN_b = \frac{1}{P_t^2P_e^2}\frac{1}{\text{FoM}}\left[\frac{\delta P_e}{P_e}\right]^{-2} . \tag{40}$$

Considering a low beam polarization P_e=10%, and a relative uncertainty of 1%, Tab. 2 gives the main

E_e (MeV)	ε_0 ($\times10^{-2}$)	$\langle E\rangle^2/\langle E^2\rangle$	A_m ($\times10^{-5}$)	FoM ($\times10^{-4}$)	N_t ($\times10^{12}$)	Δt (mn)
5	0.62	0.484	1470	0.49	3.18	9.6
10	1.74	0.470	1382	2.55	0.61	1.6

Table 2: Some characteristics of the measurement of a 10% beam polarization with a 1% relative uncertainty, at two different beam energies and an average beam current of 1 nA.

characteristics of a measurement considering an optimized polarimeter as determined in the previous sections. Noting I the average beam current, the duration Δt of a measurement is obtained as

$$\Delta t = \frac{N_t\, e}{I} \tag{41}$$

where e is the elementary electrical charge. The measurement time is reported in Tab. 2 for an average current of 1 nA. While the beam polarization of the final experiment is unknown, the chosen example of a small polarization together with a very good relative uncertainty can be considered as a worst-case scenario. Even with such unfavorable conditions, the measurement time remains quite reasonable and competitive.

6 Conclusion

Many fundamental physics experiments require an accurate knowledge of the polarization of the incident beam. This is achieved with a polarimeter apparatus such as Mott or Compton scattering polarimeters. The Compton transmission polarimeter is based on the absorption of circularly polarized photons within a polarized target, and is composed of three main elements: a radiator, an analyzer, and a calorimeter.

The first part of the project was to optimize the geometry of the calorimeter, with respect to the radius and the length of a BGO crystal. According to this study, an optimized BGO crystal would have a 3.5 cm radius and a length larger than 18 cm. The second part of the project was to optimize the length of the analyzer, optimizing the Figure of Merit. Accordingly, the optimized length of the analyzer would be 8.0 cm for the energy range of interest. The third part of the project was an evaluation of the radiation damage on the BGO crystal, with respect to the incident electron beam. Depending on the exposure time and the characteristics of the beam in the final experiment at BNL, further studies are required to control radiation damages.

The conceptual design represented on Fig. 27 has been obtained according to the optimization of each components.

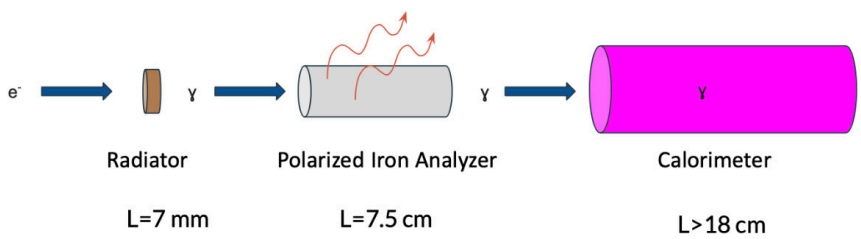

Figure 27: Conceptual design of the Compton transmission polarimeter.

A Experimental characterization of a BGO crystal

The purpose of this study is the determination of the resolution of a candidate BGO crystal for high energy muons originating from the cosmic radiation environment. Indeed, when a very high energy particle arrives in the upper atmosphere, it collides with the nuclei of the atmosphere matter and produces particles which in turn also interact, leading to a shower of particles. Among these secondary particles are short-lived charged π-mesons which decay into $\mu^{\pm}$. On the one hand, the benefit of using high-energy $\mu^{\pm}$ is to expose the crystal to high energy deposits, inaccessible with conventional radioactive sources. On the other hand, the experimental difficulty concerns the selection of these high-energy $\mu^{\pm}$ and the restriction of the length of the crossed crystal material which control the energy deposit.

A.1 Description of the experiment

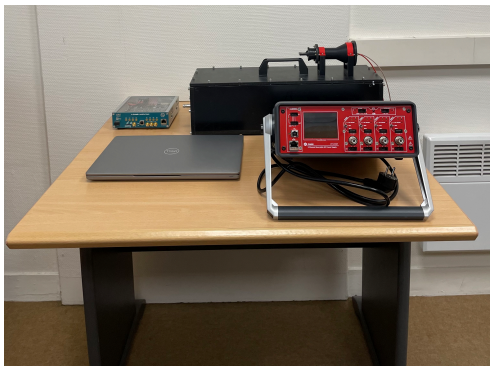

Figure A.1: Experimental setup composed by a ligth-tigth box, a wavecatcher, a HV power supply and a labtop

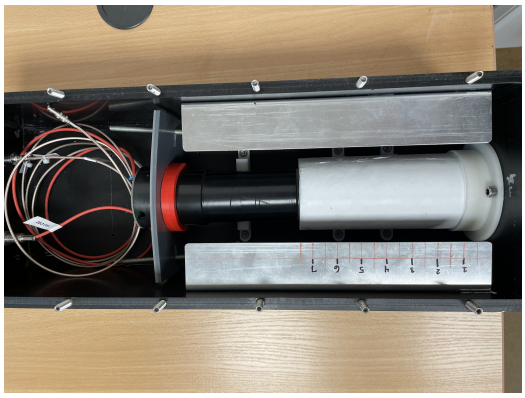

Figure A.2: Experimental arrangement of the BGO crystal and the PMT within a light-tigth box.

The experimental setup (Fig. A.1) consists of a ligth-tigth box, a wavecatcher, a HV power supply and a labtop. The HV power supply delivers high voltage (1400V) to the PMTs of the BGO and the scintillator. The wavecatcher is connected to the crystal and the labtop. It receives current and voltage from the crystal and treat the data by wrinting it in binary language. The labtop provides us code in order to decode the binary text. The ligth-tigth box consists of a BGO crystal, wrapped into a light diffusive teflon envelope, and connected to a photomultiplier tube (PMT) through a silicon patch which ensures the optical coupling. The assembly (Fig. A.2) is disposed inside a box which can be closed to protect the PMT from direct light exposition. In order to restrict the passage of muons in the crystal to a limited range of directions, a small scintillator read by a PMT is installed on top of the box. The

coincidence between a scintillator and a crystal signal defines a good $\mu^{\pm}$ event candidate. The coincidence is searched within a minimum time duration (time width of the coincidence window) to ensure that the same particle triggers both the scintillator and the crystal. Events are registered by the acquisition system for each coincidence within the coincidence window. The data consists of the shape of the signal over a duration of 1 μs, similarly to an oscilloscope. They are analyzed off-line to provide the spectra of the energy deposit in the crystal. The full experimental setup comprises:

- a BGO crystal, R=3.5 cm and L=15 cm;
- a desktop High-Voltage (HV) power supply DT1470ET;
- a R2154 Hammatsu PMT;
- a wavecatcher data acquisition system;
- a thin scintillator coupled to its PMT;
- HV and signal cables;
- a light-tight box;
- a portable labtop to control the different systems, register data, and ultimately analyze them.

A.2 Crystal signal analysis

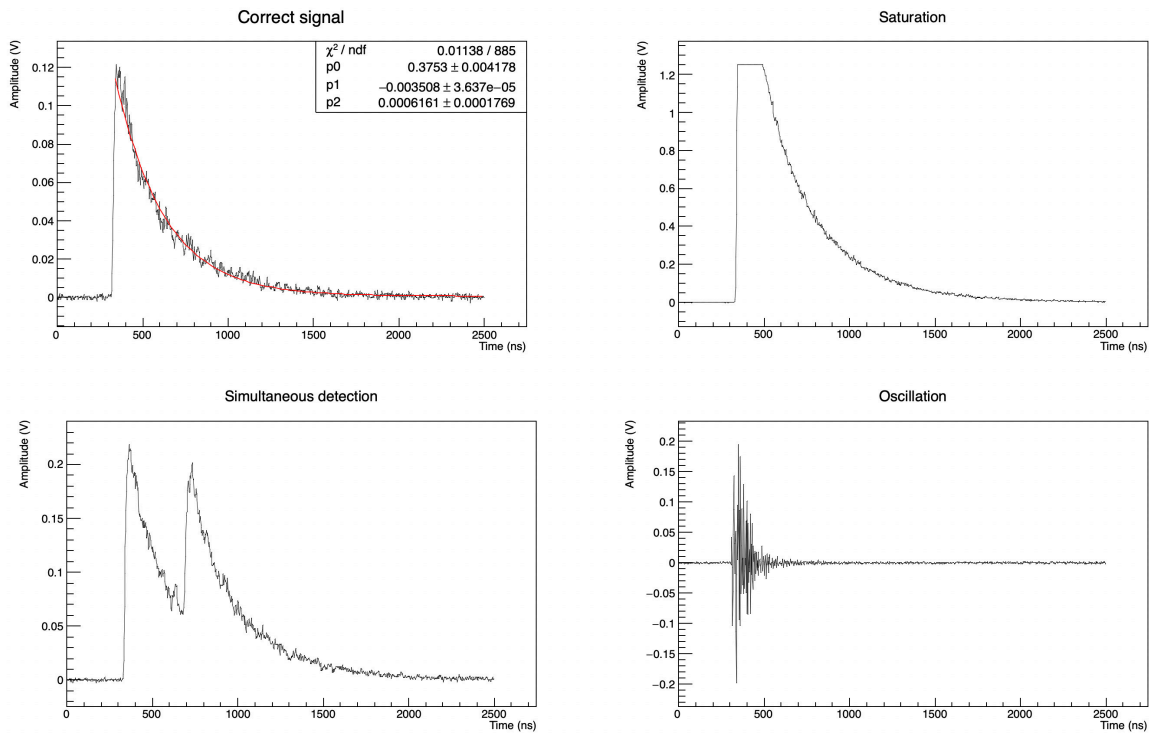

Figure A.3: Examples of the different signals registered by the wave-catcher: appropriate BGO signal (upper left panel); partially saturated signal (upper right panel); pile-up (lower left panel); electronics oscillation (lower right panel).

When a muon hit the BGO crystal, we observe a typical BGO signal (Fig. A.3 upper left panel) with an exponential decrease of the signal amplitude. In order to put in an automatic analysis of the crystal signals, we define the following set of parameters:

- t_0, the starting time of the signal;
- t_{max}, the time stamp of the maximum signal amplitude;
- t_{min}, the time stamp of the minimum signal amplitude;
- t_r=t_{max}-t_0, the rising time of the signal;
- τ, the constant decay time of the signal;
- A_{max}, the maximum signal amplitude;
- A_{min}, the minimum signal amplitude;
- S_A, the signal amplitude integrated over its duration;
- S_0, the local zero signal which may fluctuate between signals.

The decay time τ of the BGO crystal is obtained from the fit of the signal starting at t_{max}. The fitting function is defined as

$$f(p_0, p_1, p_2, t) = p_2 + p_0 e^{p_1 t} \tag{42}$$

where (p_0, p_1, p_2) are deduced from the fit with τ=$-1/p_1$. Such automatic analysis of the data assumes that a relevant and ideal signal shape. It is therefore necessary to ensure that the signal parameters are all within an acceptable range of values to make sure of the selection of appropriate signals. Different signal types have been observed which can be classified using the previously defined parameters:

- saturated signal : if the muon have too many energy, we observe a saturation for the amplitude of the signal due to the electronic stuff. As a consequence, we can't fit this signal. If we find A_{max} several times for one signal, then the signal is rejected.
- pile-up signal : This event corresponds to the detection of two muons during the data acquisition. It's a super rare event (0.1%). It means that two muons are getting through the scintillator and hit the crystal during the window time. We first obtain A_{max} of the signal. If we find in the signal an amplitude superior to $0.5A_{max}$ and far from the bin of A_{max}, the signal is rejected.
- electronics background signal : The last signal is due to the electronics of the experiment. We obtain S_0 of the signal. If A_{min} is negative and superior to $10S_0$, then the signal is rejected.

After this treatment of data, we manage to keep only good signals, and obtain the set of histograms shown in Fig. A.4.

A.3 Determination of the crystal resolution

Following the previous analysis, only appropriate signals are kept for the determination of the crystal resolution. The signal integral distribution of selected events is shown in Fig. A.5. Considering our experimental setup, the observed distribution results from the convoluted effects of several contributions:

- the intrinsic energy resolution specific to the BGO crystal;
- the fact that the experimental configuration allows a variation of the path length (that is the energy deposit) of cosmic rays inside the crystals;
- the fact that cosmic rays have an intrinsic distribution in energy and angle.

Each contribution have to be modeled in order to fit the histogram. The resolution effects are represented by a Gaussian distribution while the cosmic ray related effects are better represented by a Crystall ball function. The final fit function is a sum of these functions and an exponential function, according to the expression (43).

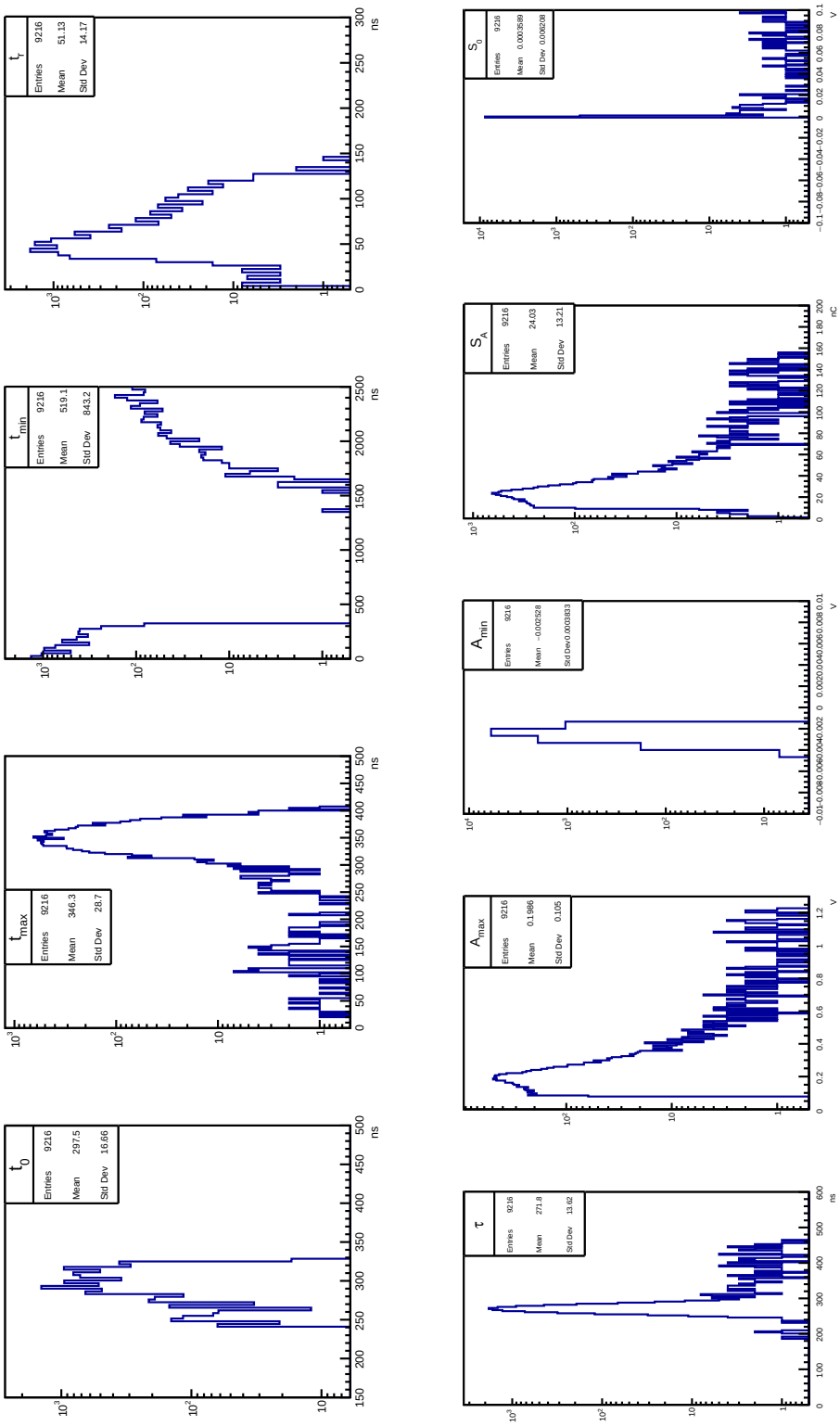

Figure A.4: Distribution of the signal parameters for coincidence cosmic events.

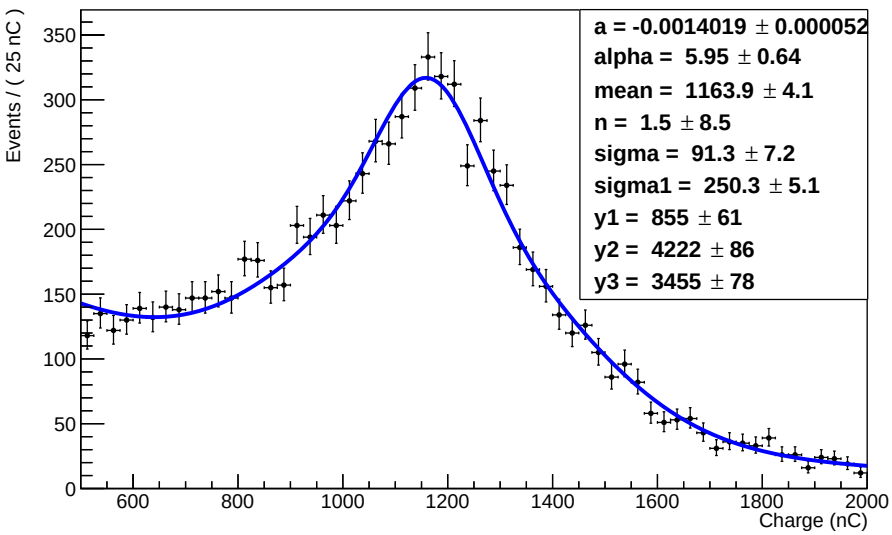

Figure A.5: Fit of the experimental signal with a Crystal ball and Gauss functions.

$$
\begin{aligned}
S_A(x, a, \mu, \sigma, \alpha, , n, \sigma_1) &= e^{-ax} + \left[\frac{n}{\mid \alpha \mid}\right]^n \left[\frac{n}{\mid \alpha \mid} - \mid \alpha \mid - \frac{x-\mu}{\sigma_1}\right]^{-n} \exp\left(-\frac{\mid \alpha \mid^2}{2}\right) \\
&+ \frac{1}{\sqrt{2\pi}} \exp\left(-\frac{(x-\mu)^2}{2\sigma^2}\right) \qquad (43)
\end{aligned}
$$

The fit of the experimental distribution is shown in Fig. A.5, which represents the fit of S_A between 600-2000 nC. The resolution Γ of the BGO crystal is obtained from the expression

$$\Gamma = \frac{\sigma}{\mu} \qquad (44)$$

where, μ is the mean of the Crystal ball function, and σ is the standard deviation of the Gaussian distribution. From the fit in Fig. A.5, the resolution of the crystal is 7.8%. Next steps would be to calibrate the wave-catcher with radioactive sources, in order to match the charge with the energy of the particle, and to better restrict the path of muons inside the crystal.

A.4 Muons energy and track length in GEANT4

We implemented in GEANT4 the geometry of the experiment in order to get the trajectory of muons inside the crystal and the energy deposited. From the positions of the muon impact points with the scintillator and with the crystal, we can obtain the track length by muons passing through the BGO crystal. The geometry of the simulated experiment is shown in Fig. A.6.

We can have an idea of the track length of the muons through the energy loss by muons in BGO such as :

$$-\frac{1}{\rho}\frac{dE}{dx} = 1.251\,\mathrm{MeV}\cdot\mathrm{cm}^2\cdot\mathrm{g}^{-1} \qquad (45)$$

which finally give

$$-\frac{dE}{dx} = 8.92\,\mathrm{MeV}\cdot\mathrm{cm}^{-1} \qquad (46)$$

We obtain the following histograms (Fig. A.7) according to the GEANT4 simulations. The first two histograms of the (Fig. A.7) represent the energy and the angle of the muons beam generated. The third histogram represents the total energy deposit in the crystal by muons. The last one is the track length

of the muons in the crystal. The number of events of the histograms fall from 100.000 to 19.762 because we keep only muons that hit the scintillator and the crystal. The average energy deposit in the crystal is 59.13 MeV and the track lenght is 7.2 cm. We can quote the track length is superior to the diameter of the BGO crystal (7 cm). Actually, the muon can hit the scintillator not perpendicularly to the crystal which lead to a track length higher than the diameter of the crystal.

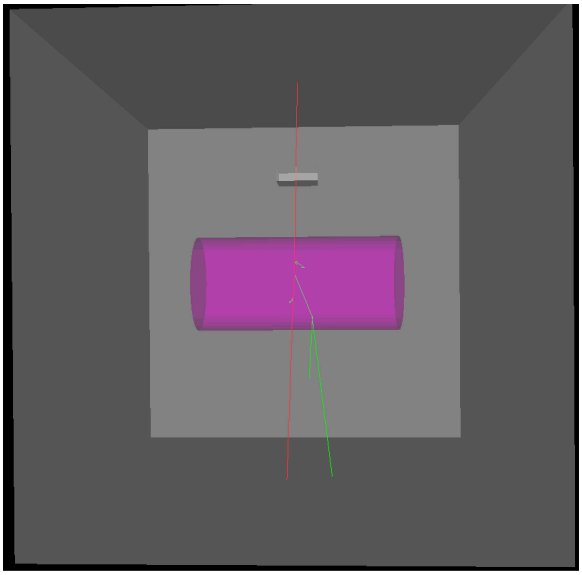

Figure A.6: Geometry implemented in GEANT4.

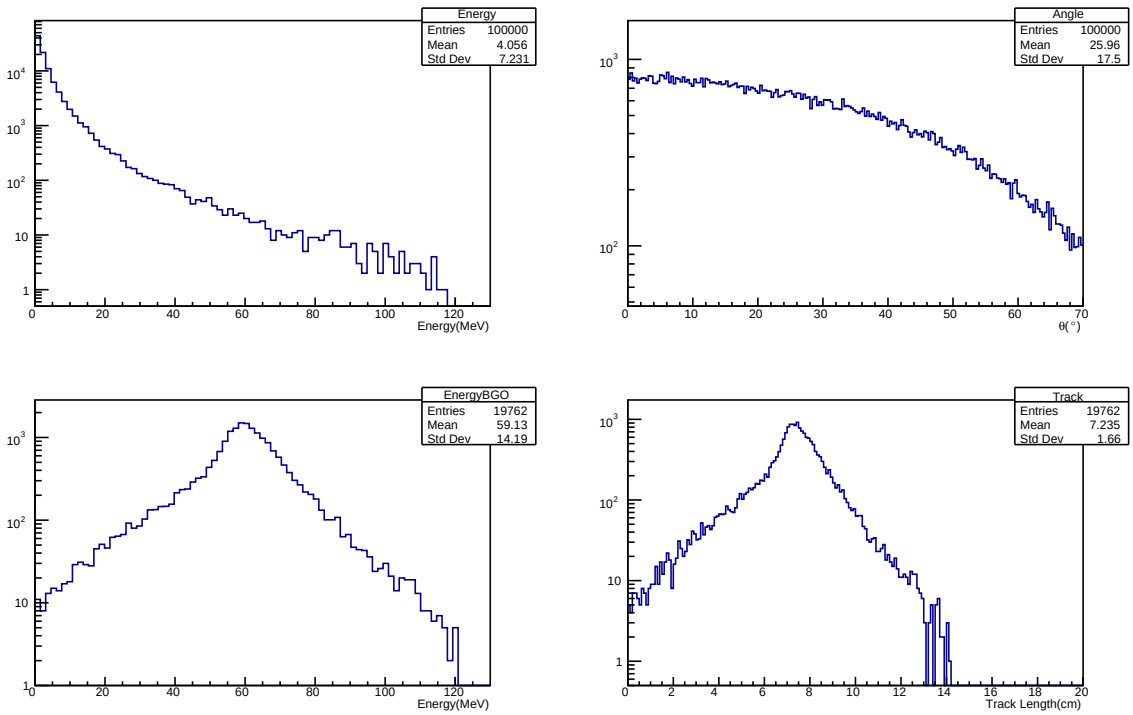

Figure A.7: Track Length and deposit energy of muons in BGO crystal.

References

[1] E. Voutier, *Private Communication.*

[2] J. Grames, E. Voutier et al. *Polarized Electrons for Polarized Positrons: a proof-of-principle experiment*, Jefferson Lab Proposal **PR12-11-105** (2011).

[3] A. Adeyemi, E. Voutier, *The calibration of the PEPPo polarimeter for electrons and positrons* , JACoW **IPAC** (2013) MOPWA078.

[4] D. Abbott et al. *Production of highly polarized positrons using polarized electrons at MeV energies*, Phys. Rev. Lett. **116** (2016) 214801

[5] Y.-S. Tsai, *Pair production and bremsstrahlung of charged leptons*, Rev. Mod. Phys. **46** (1974) 815.

[6] F. Biggs, R. Lighthill, *Analytical approximations for x-ray cross sections III*, Preprint Sandia Laboratory **SAND 87-0070** (1988).

[7] R. Barday et al. *Compton transmission polarimeter for a very precise polarization measurement within a wide range of electron currents* , J. Phys. Conf. Ser. **298** (2011) 012022.

[8] E. Voutier, *PEPPo experimental and false asymmetries*, PEPPo technical Note **TN-14-01** (2014).

[9] S. Agostinelli et al. *GEANT4 - a simulation tool kit*, Nucl. Inst. Meth. A **506** (2003) 250.